

Sensitivity of rainfall and submonthly oscillations to moist physical processes schemes on Hainan island in autumn



Qingwen Ye^{a,b}, Jiangnan Li^{a,*}, Fangzhou Li^a, Jialin Luo^b, Zixi Ruan^a

^a School of Atmospheric Sciences, Guangdong Province Key Laboratory for Climate Change and Natural Disaster Studies, Sun Yat-Sen University, Guangzhou 510275, PR China

^b Zhuhai Meteorological Service, Zhuhai 519099, PR China

ARTICLE INFO

Keywords:
Precipitation
Moist physical processes
Submonthly oscillations
WRF

ABSTRACT

In the autumns of 2010 and 2011, consecutive periods of heavy precipitation occurred in Hainan Island. Two groups of monthly-scale simulation experiments were conducted using the Weather Research and Forecasting model. Sensitivity of rainfall and submonthly oscillations to cumulus parameterization and cloud microphysical schemes were evaluated. Due to that the experiment combining the Tiedtke cumulus parameterization scheme and the WDM6 cloud microphysical scheme could reproduce submonthly oscillation characteristics, which showed the higher skill scores of the precipitation simulation than other experiments. Because the Tiedtke scheme is an overall mass flux convection scheme that describes various types of convection, the Grell-Devenyi scheme does not consider the shallow convection, which affects its simulation performance on submonthly oscillations and rainfall. However, in the same cumulus parameterization scheme, different microphysics schemes also have an impact on simulation performance. Experiments that failed to simulate the characteristics of submonthly oscillations exhibited a lower skill scores of precipitation simulation.

Interactions of moist physical processes and submonthly oscillations led to the occurrence and development of two consecutive heavy autumn precipitation events on Hainan Island. Submonthly oscillations resulted in a significant effect on the two strong autumn precipitation events, but dominant frequency modes of submonthly oscillations, oscillation characteristics, and propagation paths differed. The autumn 2010 rainfall was dominated by the 8–15-day quasi-biweekly oscillations. The autumn 2011 rainfall was dominated by the 3–10-day synoptic-scale oscillations.

1. Introduction

From September to October, Hainan Island (HNI) is in the retreat period of the South China Sea (SCS) monsoon, and the weather system becomes more complex and changeable. The variability of September–October rainfall on HNI is distinct from that of most of South China, the Indochina Peninsula, and most of the SCS (Feng et al., 2013). Precipitation mainly occurs on May–October on HNI, with peak value on autumn (Xiao et al., 2013). After mid-September, it is the alternating period from summer to winter over the Southern China and the northern South China Sea area. Cold and warm weather systems often meet and produce convection. The high- and low- altitude condition is favorable for frequently regional heavy rainfalls during this period (Feng et al., 2016). In the autumns of 2010 and 2011, consecutive periods of heavy precipitation occurred on HNI. Based on statistical analysis, our previous study (Li et al., 2017) showed that the

heavy precipitation in 2010 was dominated by 8–15-day quasi-biweekly oscillations but dominated by 3–10-day synoptic-scale oscillations in 2011. Based on successful monthly-scale simulation experiments, we found out that three categories of graupel has a dramatic influence on the two consecutive precipitation intensity (Li et al., 2019). In this paper, we evaluate sensitivity of the two consecutive precipitation and atmospheric oscillations to CP schemes and CM schemes further by using the WRF model.

The intraseasonal oscillation (ISO) is mainly contributed by 10–20 days oscillation and 30–60 days oscillation. It was first discovered by Madden and Julian (1971) over the tropical region. It is an important periodic signal that affects tropical atmospheric circulation and precipitation. Soon, however, 2.5–6 days (Blackmon, 1976), 3–8 days (Lau and Lau, 1990), and 7–15 days (Vitorino et al., 2006) submonthly oscillations (SMO) were also found at tropical and extratropical latitudes. Various studies have also shown that the rainfall in

* Corresponding author at: School of Atmospheric Sciences, Sun Yat-sen University, Guangzhou 510275, PR China.
E-mail address: essljn@mail.sysu.edu.cn (J. Li).

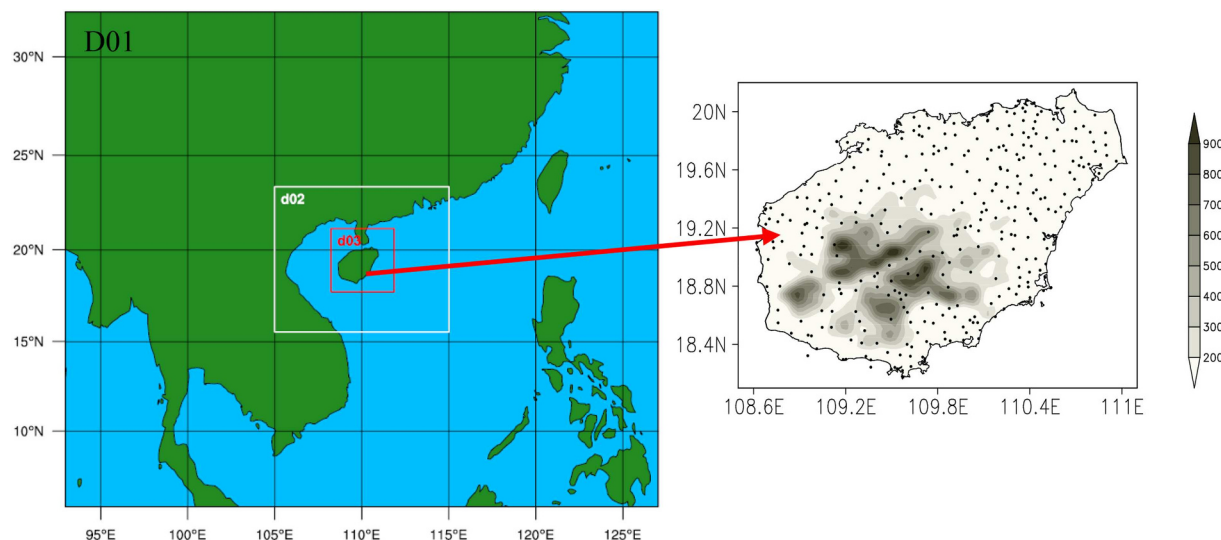


Fig. 1. The experiment domain setting and the location of 340 Hainan precipitation stations and topography (m).

Table 1
Designing of experiments.

Experiment identifier	CP scheme (D01 D02)	CM scheme (D01 D02 D03)
T1	Tiedtke (Group T)	Lin
T2		WSM6
T3		MORRISON
T4		WDM5
T5		WDM6
G1	Grell-Devenyi(Group G)	Lin
G2		WSM6
G3		MORRISON
G4		WDM5
G5		WDM6

Southeast China is closely related to ISO (Chen et al., 2001; Zhu et al., 2003; Zhou et al., 2006; Zhou et al., 2006; Zhang et al., 2009; Ren et al., 2013; Abhilash et al., 2014; Li et al., 2014; Li and Zhou, 2015; Chen et al., 2015; Gao et al., 2016; Sun et al., 2016). For example, Chen et al. (2001) observed that the flooding in the Yangtze River Basin (YRB) in the summer of 1998 was related to the convergence of low-latitude and middle-high latitude low-frequency cyclones in the vicinity of the YRB. Sun et al. (2016) indicated the role of ISO in the persistent and extreme precipitation over the YRB in June 1998. Wang et al. (2018) showed the effect of ISO on onset of SCS summer monsoon sooner or later. The rainfall over the Yangtze and Huai River basin (YHRB) during the summer of 1991 was also dominated by 15–35 days of oscillations (Mao and Wu, 2006). The location and strength of ISO play a decisive role in controlling the severity and duration of rainfall events over South China (Li and Zhou, 2015). The ISO also affects tropical cyclone tracks over the western North Pacific (Wang et al., 2019).

Numerical simulation is an important method in the studies of the ISO. However, simulation of ISO is a major problem in state-of-art models (Lin et al., 2006; Ren et al., 2019). Numerous atmospheric general circulation models (AGCMs) fail to reproduce the features of the amplitude and propagation of the ISO (Slingo et al., 1996; Jones, 2000; Sperber, 2004; Zhang, 2005; Kim et al., 2009; Li et al., 2014). AGCM has its own set of limitations, such as the coarse resolution at which they are conducted (Hayashi and Golder, 1986). The total errors in numerical forecasts are significantly related to the capability of the forecast model to accurately predict the ISO. Improved numerical simulations of the ISO could substantially increase the accuracy of weather forecasting (Maloney and Hartmann, 2000a, 2000b), since the

ISO effect is pivotal to predicting both the weather and climate (Zhang, 2013). A variety of studies also showed that the cumulus parameterization (CP) scheme employed in the model is critical to simulating ISO (Slingo et al., 1996; Chao and Deng, 1998; Wang and Schlesinger, 1999; Maloney and Hartmann, 2001; Jia et al., 2010; Hu et al., 2011; Ham and Hong, 2013).

The total intraseasonal variance of precipitation is too weak in most of the models. The AGCMs cannot well capture the atmospheric variance associated with the ISO, which also leads to poor simulation precipitation (Lau and Poshay, 2009; Chen et al., 2011; Srinivas et al., 2013; Goswami and Goswami, 2017). Regional climate models (RCMs) are tools for describing regional climatic conditions; therefore, RCMs have been increasingly applied in monthly (or seasonal)-scale high-resolution simulations (Wang et al., 2003; Pal et al., 2007; Kim and Hong, 2007; Segele et al., 2009, 2015; Seol and Hong, 2009; Liu and Wang, 2011; Jang et al., 2016). The WRF model can reproduce weather processes and regional climate (Heikkilä et al., 2011; Marteau et al., 2015; Jones and Carvalho, 2014; Li et al., 2016; Mohan and Sati, 2016; Boulard et al., 2015, 2017; Raghavan et al., 2016; Gbode et al., 2019; Moya-Álvarez et al., 2019).

The WRF model can also well reproduce the Indian summer monsoon ISOs at gray-zone resolution (Chen et al., 2018). Chen et al. (2017) successfully simulated one October ISO event by using WRF with new parameterization of surface heat fluxes. Moist physical processes (MPP) in the WRF model are handled by using the CP scheme and the cloud microphysical (CM) scheme. Therefore, the CM scheme also is important for high-resolution climate simulation. However, less research aims at evaluating the influence of the CM scheme on climate simulation. A range of ISOs that affect south China, ranging from the 8–15 days SMO in 2010 to the 3–10 days SMO in 2011. Previous studies mainly focused on summer rainfall and the 30–60- or the 10–30-day ISOs and paid less attention to autumn rainfall with a period of less than 10-day ISO. A period of less than 10 days of SMO is also important. For example, the dry and wet regions in East China feature significant 2–16-day SMO (Li and Ju, 2009). Rainfall in the South China Sea (SCS) involves a 2–8-day SMO (Li et al., 2011). Two dominant frequency modes of the summer 2003 heavy rainfall in East China include the 10–20- and 3–8-day variations (Liu et al., 2014).

Based on our previous research foundation (Li et al., 2017, 2019), the focus of this paper will be on evaluating the sensitivity of rainfall and SMO in autumn to MPP. Section 2 presents the data used and the experimental setup for the WRF simulations. Section 3 discusses the simulated precipitation validation. Section 4 focuses on the role of SMOs. Section 5 summarizes the results.

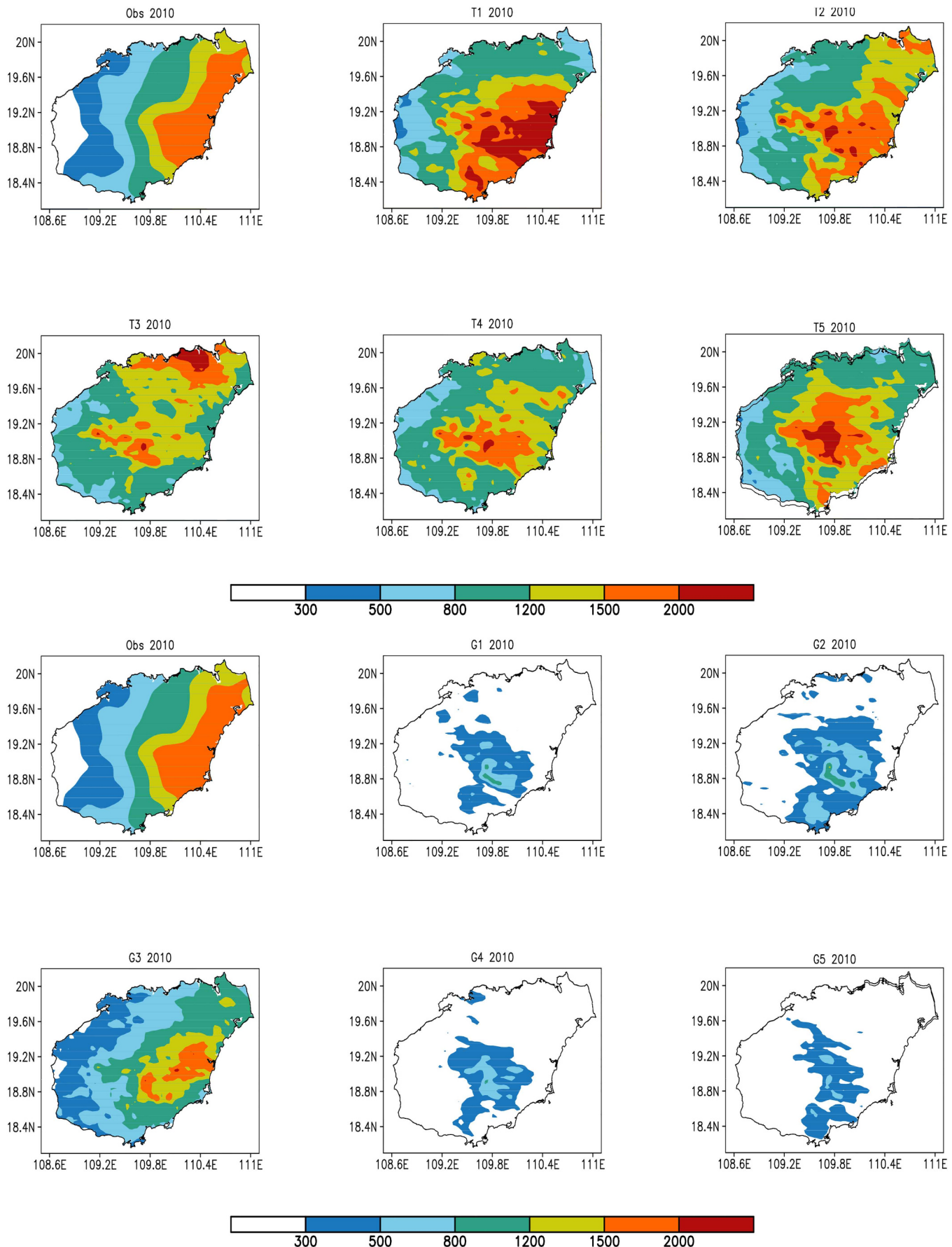


Fig. 2. Accumulative precipitation of 338 observation sites and experiments (from D03) from September 25 to October 24, 2010 (mm).

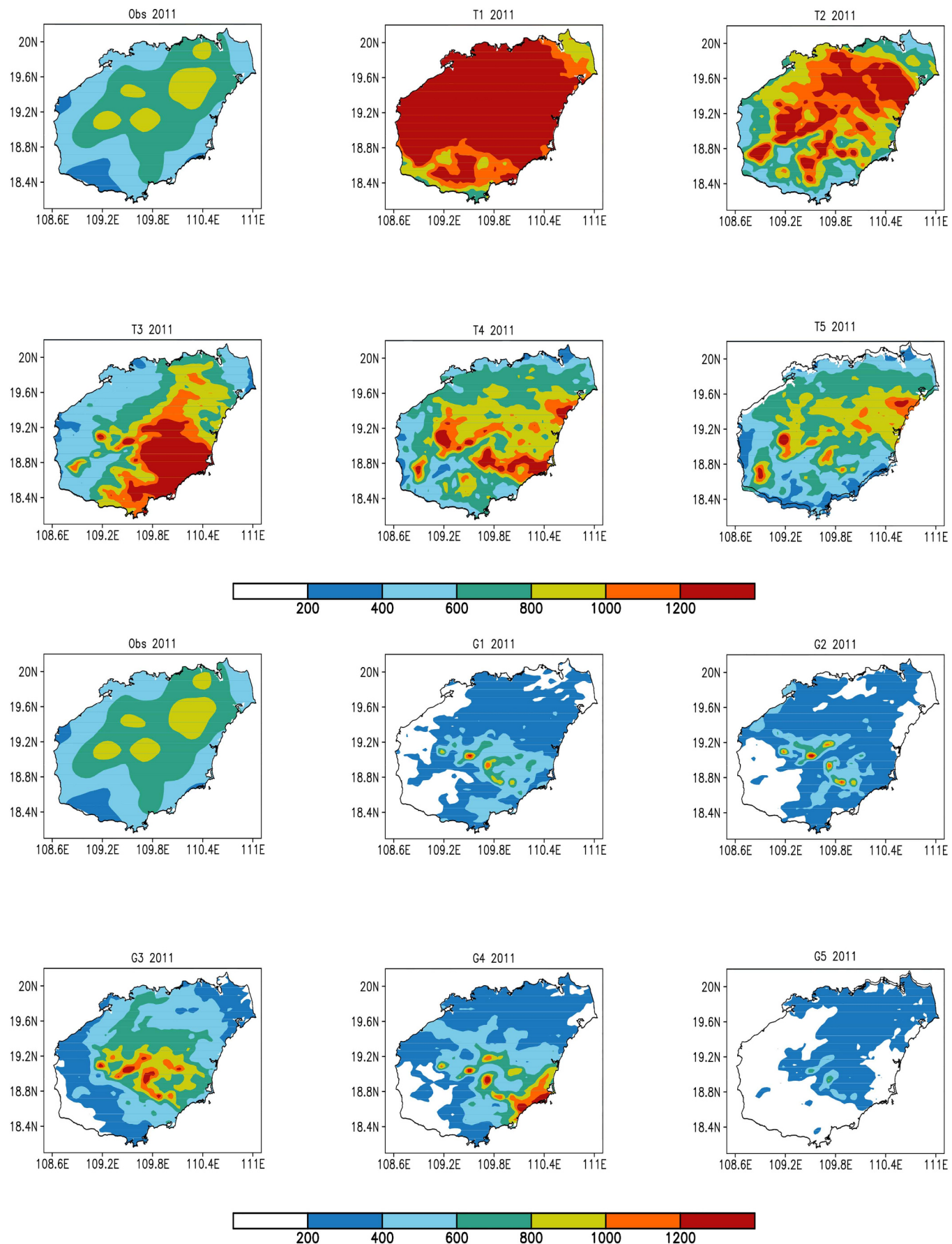


Fig. 3. Accumulative precipitation of 332 observation sites and experiments from September 25 to October 24, 2011 (mm).

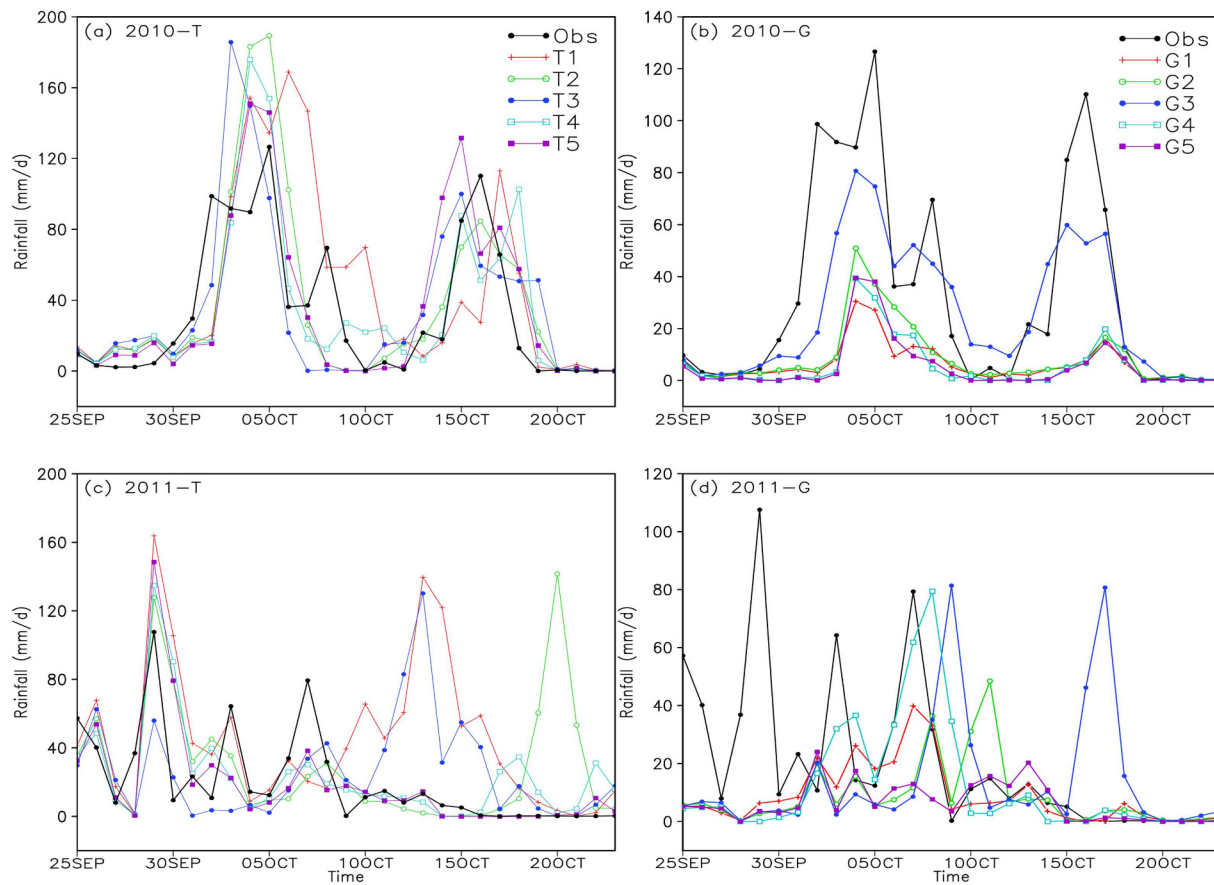


Fig. 4. Time series of Hainan Island regional ($E108.5^{\circ}$ - 111.1° ; $N18.1^{\circ}$ - 20.2°) average daily rainfall (mm) from the observation and simulations (from D03).

2. Experimental design and data

Two groups of simulation experiments were conducted for each of the heavy rain processes in autumn by using the Advanced Research WRF model version 3.7 (Skamarock and Klemp, 2008). The basic experiment settings are as follows: Mercator map projection and three-level mesh nesting (Fig. 1). The grid intervals of D01, D02 and D03 are 30, 10, and 3.333 km while the numbers of grid points are 120×100 , 106×88 , and 115×115 respectively. 30 non-equidistant σ levels were considered in the vertical direction. The top of the model is 50 hPa. The Yonsei University boundary layer scheme (Hong et al., 2006), Noah land-based scheme (Chen and Dudhia, 2001), RRTM long-wave radiation (Mlawer et al., 1997), and Dudhia short-wave radiation scheme (Dudhia, 1989) were adopted for each experiment. As for the D03, no CP scheme was used. The mode integration period was from 00:00 on September 25 to 18:00 on October 24 (UTC time) in 2010 and 2011.

Many studies (e.g., Huang et al., 2009; Yu et al., 2011; Huang et al., 2016) have shown that the mass flux cumulus convection scheme has better performance on the precipitation simulation over southern China. To investigate the sensitivity of the SMO to MPP, the Tiedtke (Tiedtke, 1989; Zhang et al., 2011) and Grell–Devenyi (Grell and Dévényi, 2002) CP schemes were selected among the mass flux schemes. For better understanding of the interaction between SMO and MPP, five different CM schemes were selected in this study: the LIN (Lin et al., 1983), WSM6 (Hong and Lim, 2006), MORRISON (Morrison et al., 2009), and WDM5 and WDM6 (Lim and Hong, 2010) schemes. Table 1 describes the design of the experiments.

The initial field data were reanalyzed by the FNL data for the NCEP/NCAR with a horizontal resolution of $1^{\circ} \times 1^{\circ}$ per 6 h. The daily precipitation data of 340 automatic observatories on HNI (Fig. 1) are used

to verify simulation results. These data have been processed by the quality control of Hainan Meteorological Observatory. The spatial resolution of the automatic observation stations is about 7 km.

3. Precipitation validation

The precipitation characteristics are shown mainly by the simulation results of the D03. In 2010 (Fig. 2), the distribution of accumulated precipitation decreased from east to west, and that in the eastern precipitation center exceeded 1500 mm. The simulated precipitation amount in Group T was higher than that in Group G, and the distributions of precipitation centers in each experiment differed. In Group G, only the G3 experiment could reproduce the distribution characteristics of precipitation, whereas the other experiments were insufficient to reflect the precipitation characteristics. Thus, the model is also sensitive to the microphysical scheme in the case where the same CP scheme is used.

The accumulative precipitation in 2011 (Fig. 3) was mainly distributed in northern HNI, and that of the center was more than 800 mm. The values in Experiments T1, T2, and T3 were all higher than the real rainfall level. The simulated precipitation intensities in Experiments T4 and T5 were closer to the real rainfall values. The simulated precipitation in northern HNI in Group G was lower than the real rainfall value. The rainfall was overestimated over the central HNI and south-eastern HNI in G3 and G4, respectively.

According to the comparison of the experimental results for Groups T and G, although no CP scheme was used in D03, the CP schemes adopted in D01 and D02 also affected the simulated precipitation in D03 owing to the two-way nesting operation. From the results of the two groups experiments, Group T exhibited a better simulation of precipitation than Group G, which presented a significantly less

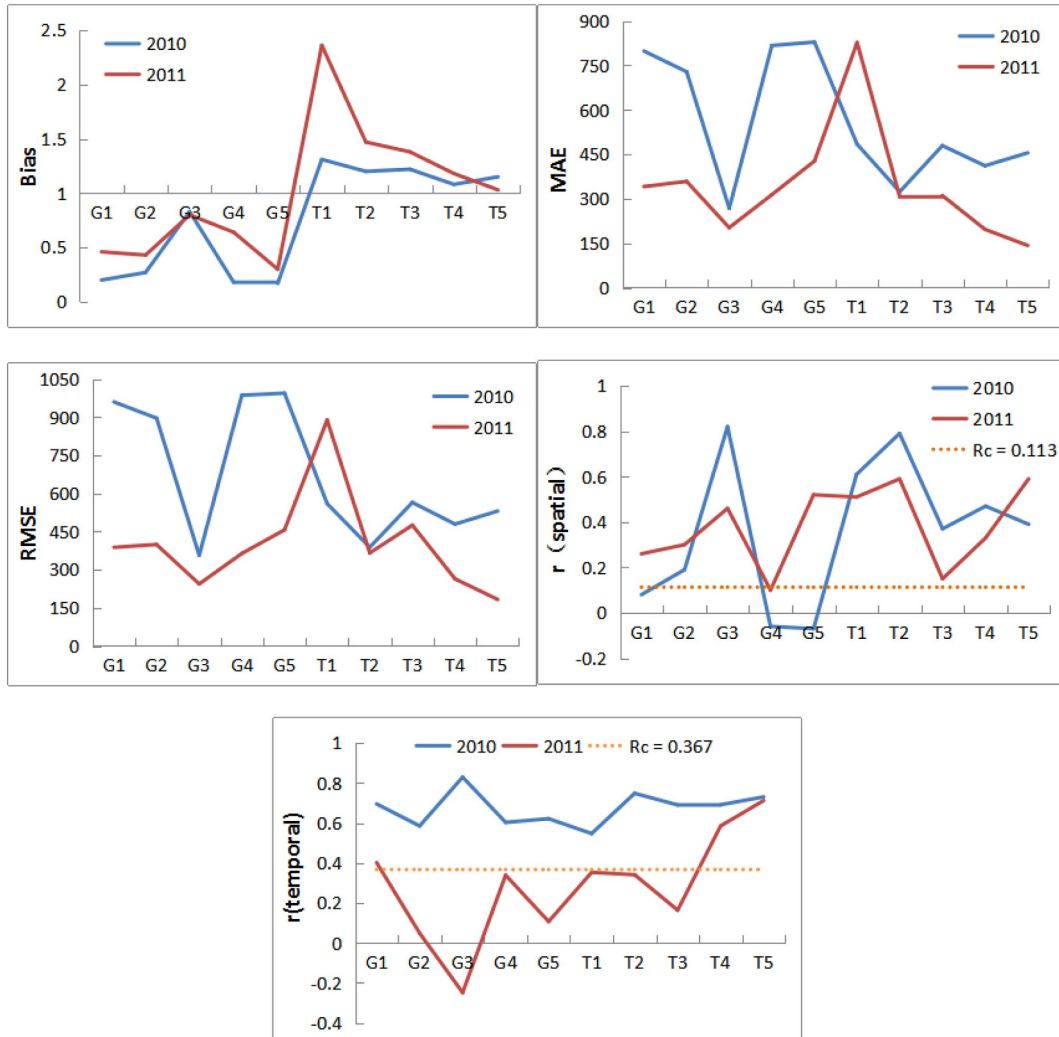


Fig. 5. Simulated precipitation (from D03) BIAS, MAE, RMSE and r (spatial, critical correlation coefficient $R_c = 0.113$), r (temporal, $R_c = 0.367$).

simulation of precipitation (Fig. 4) that cannot reflect the actual precipitation. In the same CP schemes, the model precipitation also showed high sensitivity to the CM schemes.

The ability to simulate the two precipitation events at monthly-scale was assessed by quantifying the magnitude bias and measuring similarity in temporal and spatial variability (Evans et al., 2012; García-Ortega et al., 2017). By virtue of inverse distance weighted, the simulated precipitation of 2010 was interpolated in 338 stations of HNI, and the simulated precipitation of 2011 was interpolated in 332 stations. The following specific indexes were selected.

$$\text{Bias} = \frac{\sum_{i=1}^n M_i}{\sum_{i=1}^n O_i} \quad (1)$$

$$\text{MAE} = \frac{1}{n} \sum_{i=1}^n |M_i - O_i| \quad (2)$$

$$\text{RMSE} = \sqrt{\frac{1}{n} \sum_{i=1}^n (M_i - O_i)^2} \quad (3)$$

The spatial and temporal similarity of precipitation is estimated by the Pearson's product-moment correlation coefficient (r):

$$r = \frac{\sum_{i=1}^n (M_i - \bar{M})(O_i - \bar{O})}{\sqrt{\sum_{i=1}^n (M_i - \bar{M})^2} \sqrt{\sum_{i=1}^n (O_i - \bar{O})^2}} \quad (4)$$

Where n is total number of comparisons, M is the modelled value and O is the observation value.

The closer the bias is to 1, the better the effect. The two years bias for group G was less than 1 (Fig. 5), that is, the simulated precipitation was less than the actual situation. Among them, the bias of G3 was about 0.8, which was the best in group G. The bias of group T was greater than 1, that is, the simulated precipitation was greater than the actual situation. Among them, T4 and T5 were closer to 1, which were the best in group T. Comparing the bias of G3, T4 and T5, the research got that T4 (1.082) was the closest to 1 in 2010 test with the best effect, followed by T5 (1.148); in 2011, T5 test (1.026) was the best. The experiment G3 had good performance on simulating the distribution of accumulated precipitation, except the bias was relatively high. Combining all kinds of the evaluations, the T5 test simulated the best.

The smaller the MAE value (Fig. 5), the better the effect. The MAE value of G3 was the lowest in 2010 tests, followed by T2, T4 and T5. In the 2011 tests, the MAE value of T5 was the lowest, followed by T4 and G3.

The smaller the RMSE value (Fig. 5), the better the effect. The MAE value of G3 was the lowest in 2010 tests, followed by T2, T4 and T5. In

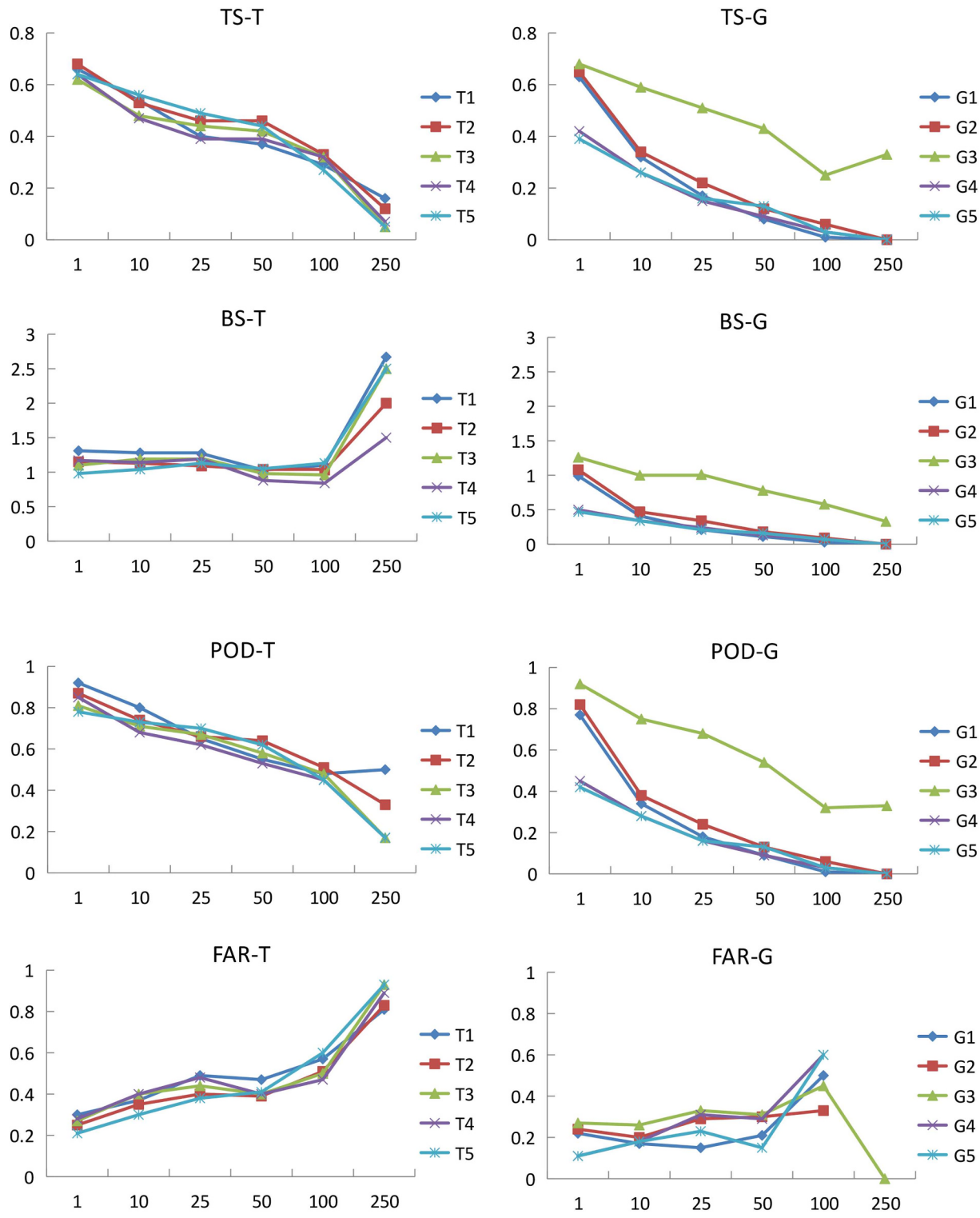


Fig. 6. Skill scores of average daily precipitation (from D03) in 2010; daily precipitation each with a threshold greater than 1, 25, 50, 100, and 250 mm/d respectively.

the 2011 tests, the MAE value of T5 was the lowest, followed by T4 and G3.

In 2010 the spatial correlation coefficients r (Fig. 5) all passed the 95% reliability test except for G1, G4 and G5, while all passed the test in 2011 except for G4. The temporal correlation coefficients r (Fig. 5) showed that the correlation between the two groups of experiments in 2010 agreed with the actual condition, that is, the correlation coefficients r of T2, T5, and G3 were all larger than 0.7. The temporal

correlation of Group T was stronger than Group G in 2011, the best correlation was noted in T5, with a correlation coefficient of 0.712.

Bias score (BS); threat score (TS); probability of detection (POD); and false-alarm rate (Hong, 2003) are defined as.

$$BS = F/O \quad (5)$$

$$TS = H/(O + F - H) \quad (6)$$

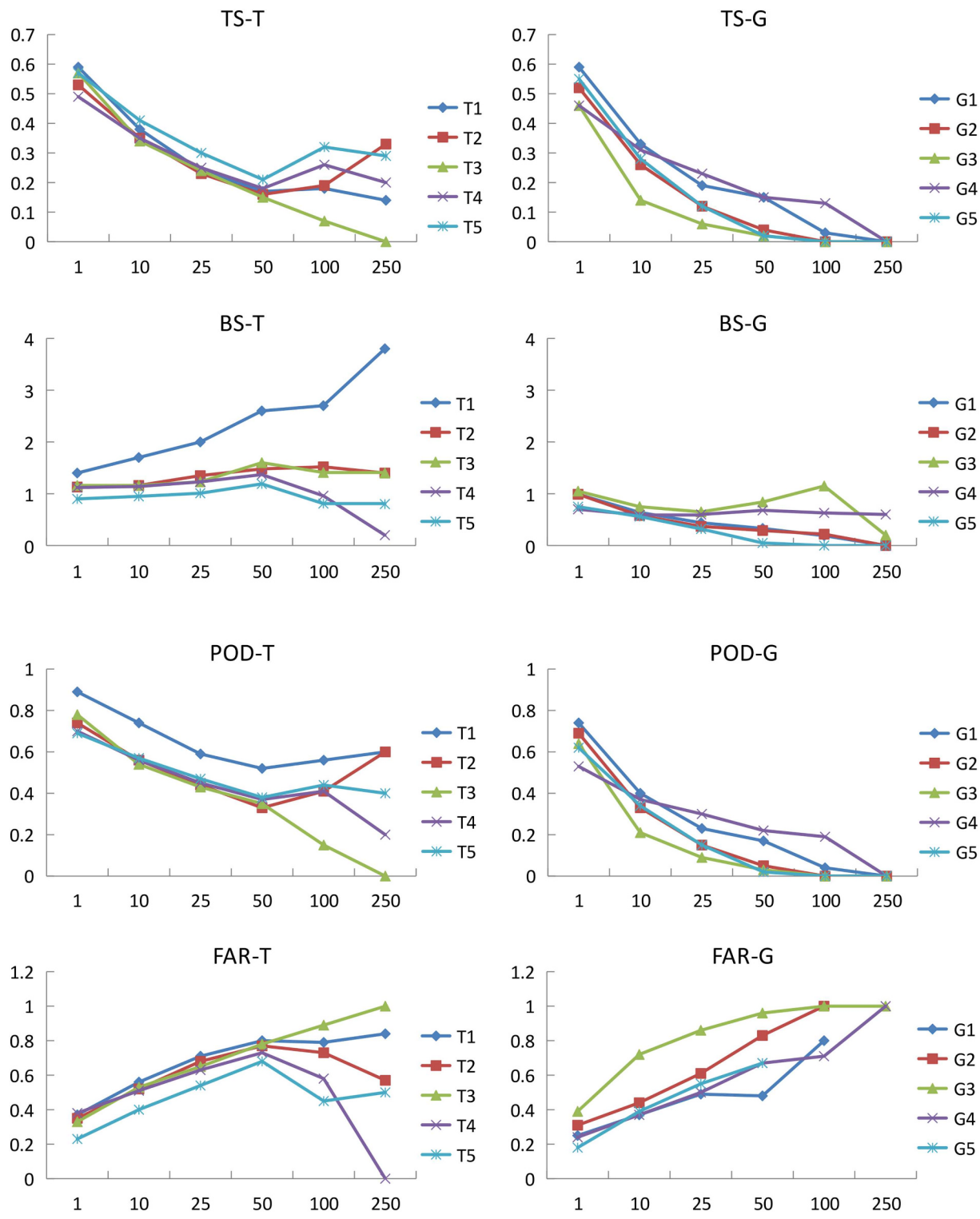


Fig. 7. Skill scores of average daily precipitation (from D03 domain) in 2011; daily precipitation each with a threshold greater than 1, 25, 50, 100, and 250 mm/d respectively.

$$POD = H/O \quad (7)$$

$$FAR = (F - H)/F = 1 - H/F \quad (8)$$

where O, F, H, and N represent the observed and model-predicted areas of rainfall exceeding a given threshold value, their intersection, and the entire region of verification (Wang et al., 2013).

The daily precipitation from September 25 to October 23 was scored with TS, and the score thresholds were 1, 10, 25, 50, 100 and 250 mm.

Then the research calculated TS, BS, POD and FAR under each threshold. Higher TS and POD values and lower FAR values indicate better simulation effect. If the FAR has no value, that is, the test does not simulate daily precipitation that is greater than the threshold (e.g. the tests G1, G2, G4, G5 in 2010 and the tests G1, G2 and G5 in 2011 did not simulate precipitation greater than 250 mm/d; in 2011, test G5 did not simulate precipitation greater than 100 mm/d). BS is the ratio between simulated points and observed points exceeding a certain

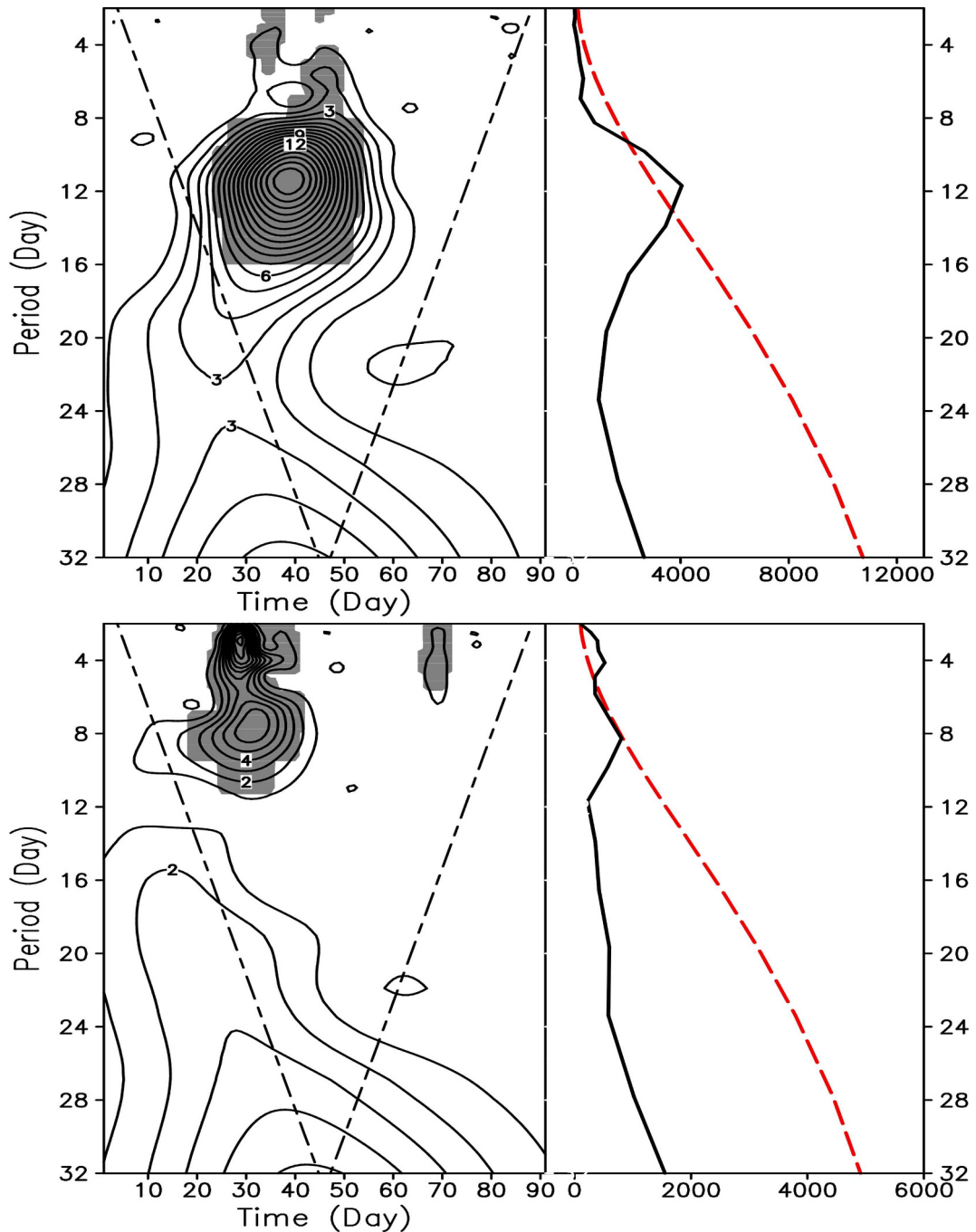


Fig. 8. The wavelet power spectrum (left panel) for the observed daily rainfall in HNI from September 1 to November 30. Up 2010; Down 2011. (Shaded areas show the 95% confidence level in 2010, the 90% confidence level in 2011). Also shown is the time average (right panel); and red lines denote confidence level. (For interpretation of the references to colour in this figure legend, the reader is referred to the web version of this article.)

threshold, and represents the proportion of simulated and observed precipitation ranges, ranging from 0 to positive infinity, with the ideal state of 1.

The TS values of group T in 2010 (Fig. 6) were consistent at each threshold. The test scores of T2 and T5 were generally higher than those of the other tests within the threshold range of 1–50 mm, and the TS values of T5 decreased within the threshold range of 100–250. The BS values of group T were all below 1.5 within the range below 100 mm. Among them, T5 is closest to 1 with the best performance; the BS values were significantly increased within the range above 250 mm/d, indicating that the simulation precipitation was significantly greater than the actual situation within the range above 250 mm/d. (See Fig. 7).

Except G3, the test scores of group G were generally worse than those of group T. Among them, the BS value was less than 1 except for the precipitation threshold of 1 mm/d, decreasing with the increase of the threshold value. That means group G was weak in simulating precipitation at each threshold, which is also one of the reasons for poor TS score.

The TS values of group T in 2011 (Fig. 6) decreased with the increase of the threshold value. Among them, the TS value of T5 was the highest, while the FAR value of T5 was generally lower, indicating that T5 was better than other tests. The scores of group G decreased with the increase of the precipitation threshold, this fact indicated that group G underestimated precipitation, especially heavy precipitation events.

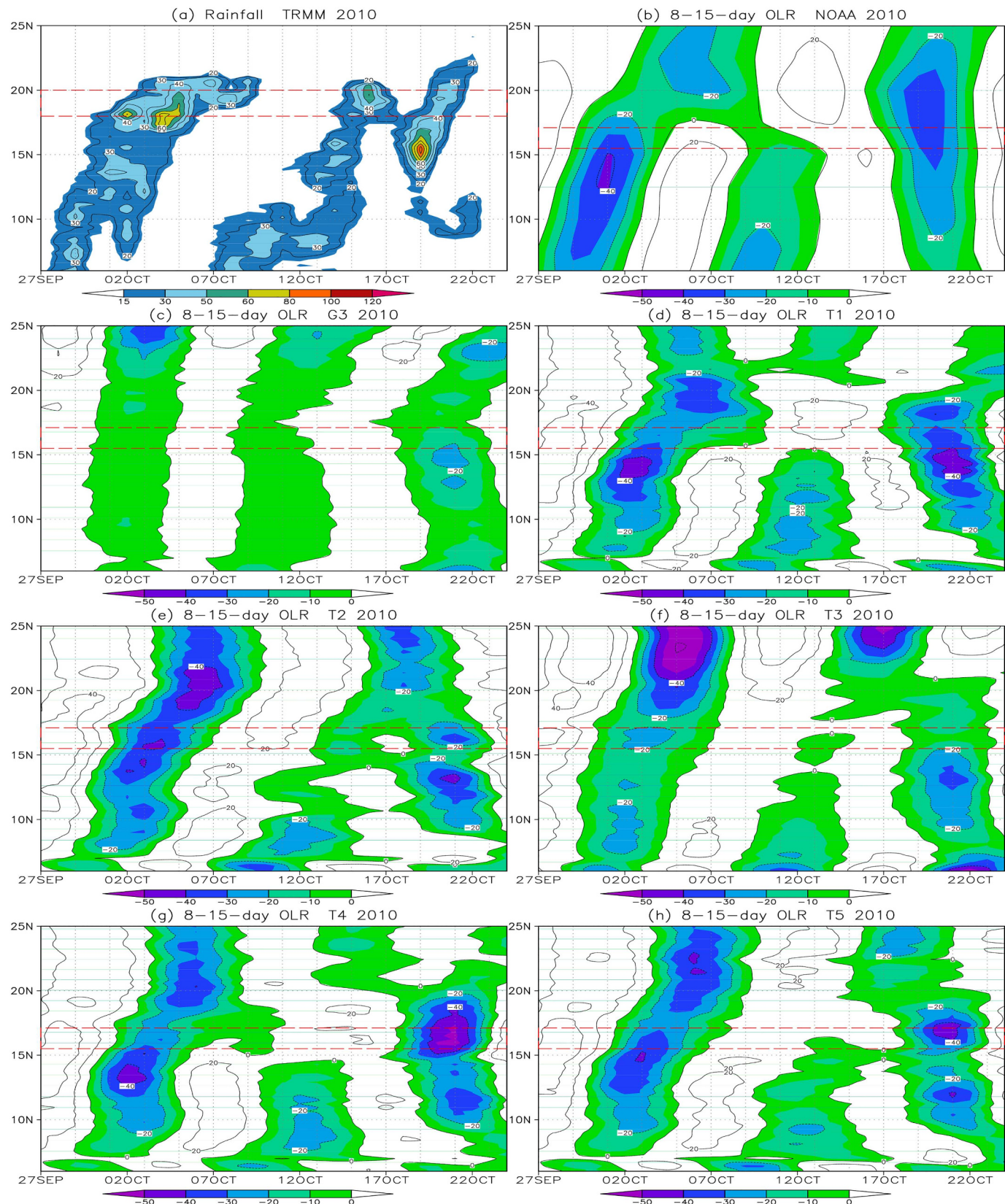


Fig. 9. Time-latitude distributions of averaged daily precipitation (mm) (from D01) and 8–15-day OLR ($\text{W}\cdot\text{m}^{-2}$) in 108°E – 110°E for 2010 (a) Precipitation; (b) NOAA; (c) Experiment G3; (d) Experiment T1; (e) Experiment T2; (f) Experiment T3; (g) Experiment T4; (h) Experiment T5. 108° – 110° E is the longitude range including Hainan Island. The red area is HNI. (For interpretation of the references to colour in this figure legend, the reader is referred to the web version of this article.)

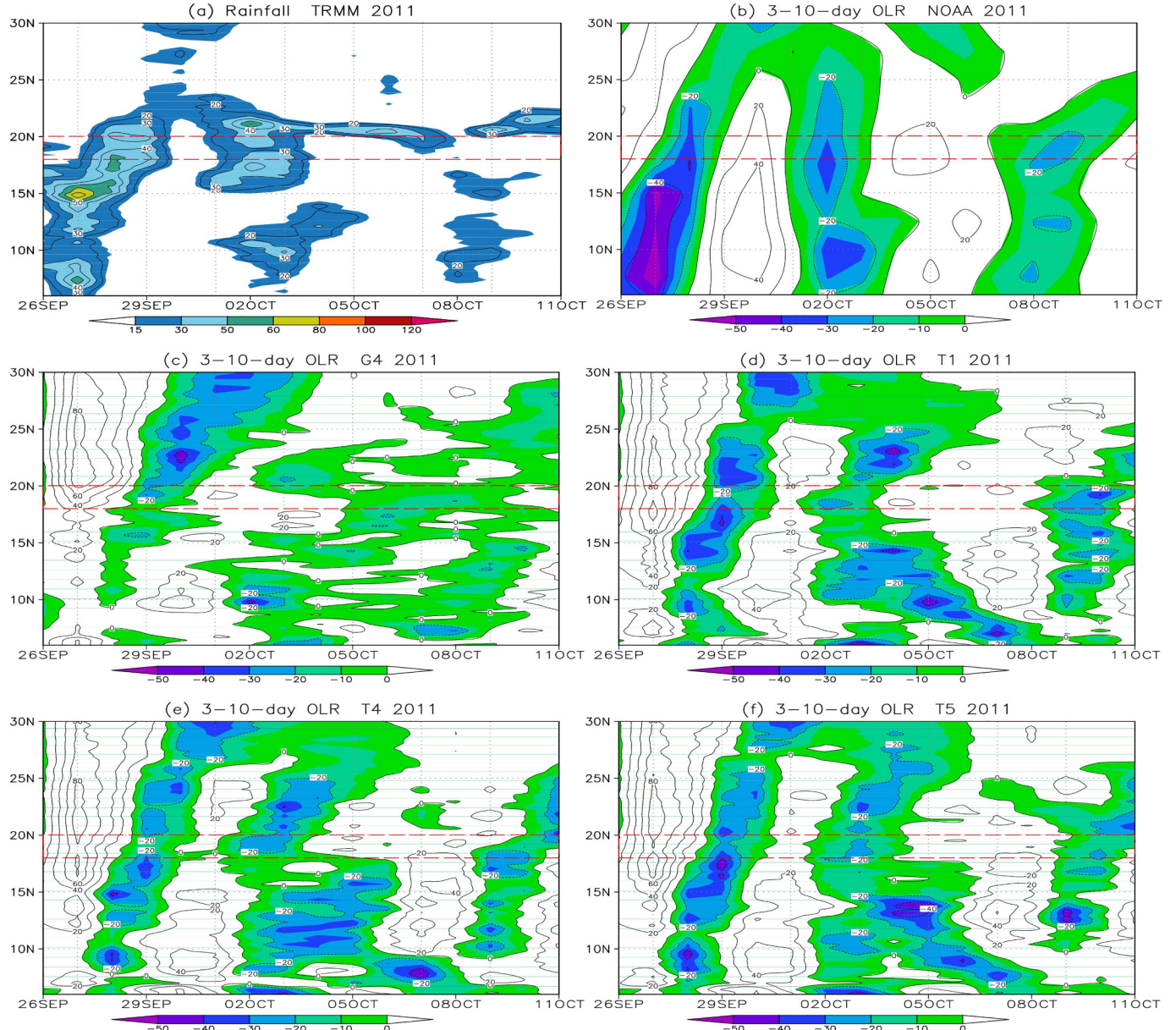


Fig. 10. Time-latitude distributions of averaged daily precipitation (mm) (from D01) and 3–10-day OLR (unit: $\text{W}\cdot\text{m}^{-2}$) in 108°E – 110°E for 2011 (a) Precipitation; (b) NOAA; (c) Experiment G4; (d) Experiment T1; (e) Experiment T4; (f) Experiment T5. 108° – 110° E is the longitude range including Hainan Island. The red area is HNI. (For interpretation of the references to colour in this figure legend, the reader is referred to the web version of this article.)

The TS values of the precipitation were 0 within the range above 250 mm/d, and the test cannot simulate the precipitation greater than 250 mm/d. It can be seen from BS that, except for T1, the BS values in group T is closer to 1, with good effect. The BS values of group G is generally less than 1, indicating that the simulated precipitation range is generally less than the actual situation. By contrast, the overall scores of T5 were better, with the best simulation effect.

Comparing the skill scores, time variation, intensities, and spatial distribution of the simulated precipitation from the two groups of experiments, experiment T5 presented the best results among the experiments for 2010 and 2011, followed by the T4 scheme. In the same CP scheme, the simulation performances of different CM schemes were quite different. The role of CM schemes on the extreme daily precipitation was obvious (Fig. 4).

4. Role of submonthly oscillations and MPP

We performed a Morlet wavelet analysis (Torrence and Compo, 1998) on average daily precipitation from Hainan's meteorological stations (Fig. 8), the autumn precipitation in 2010 on HNI presented a significant period of 8–15 days passing the 95% confidence level, while the autumn precipitation in 2011 also exhibited a period of 3–10 days passing the 90% confidence level. The northward propagation processes of the two torrential rains in 2010 (Fig. 9a) is correlated to the 8–15 days oscillation northward propagation processes of the outgoing longwave radiation (OLR) (Fig. 9b). The northward propagation processes of the two precipitation periods of 2011 (Fig. 10a) is greatly consistent with the 3–10 days oscillation northward propagation of OLR (Fig. 10b), indicating that the precipitation in 2010 was mainly affected

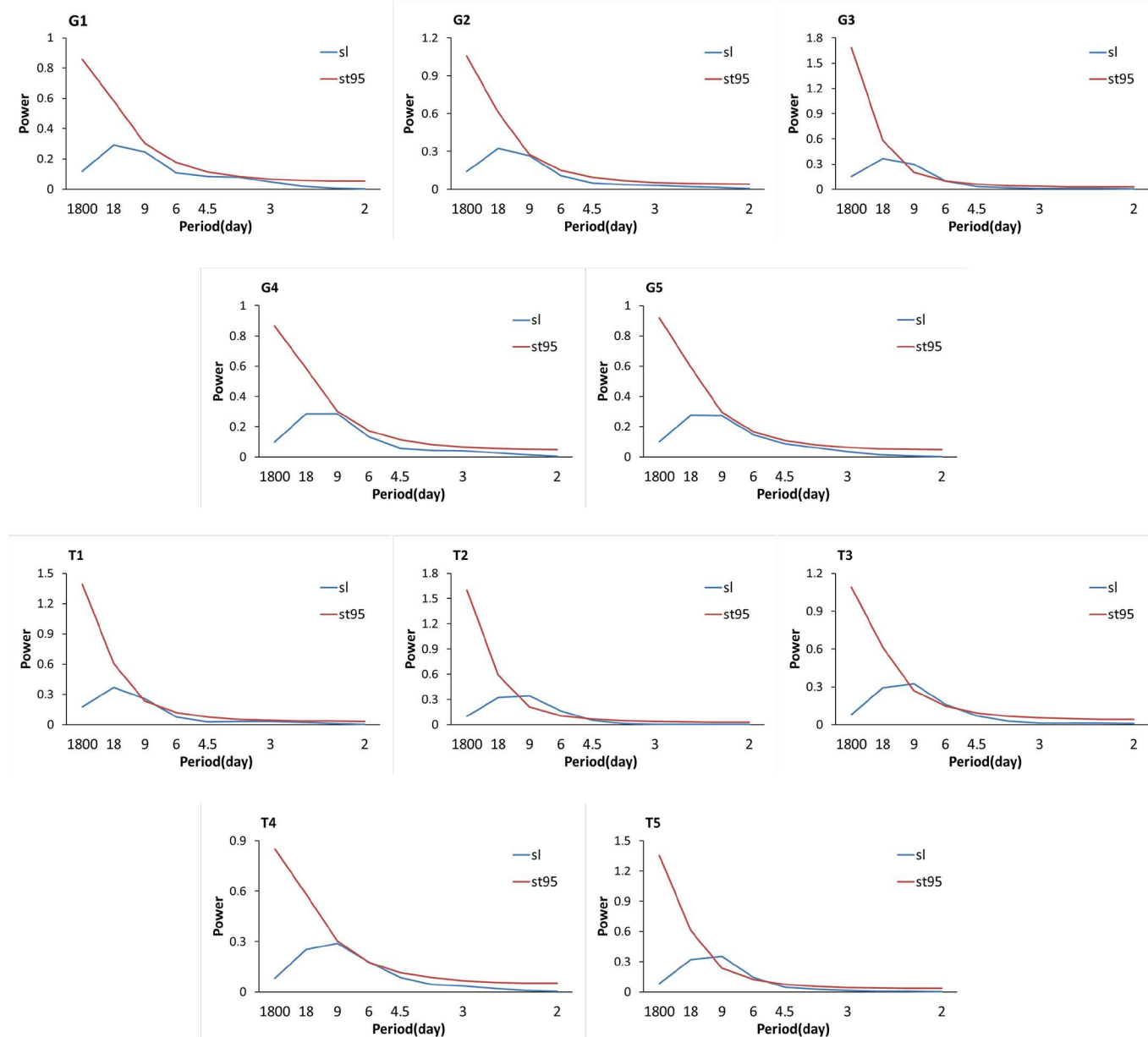


Fig. 11. Power spectrum for average daily simulated precipitation (from D03) from September 25 to October 24, 2010. (The blue line is the power spectrum, and the red line is the red noise test spectrum , 95% confidence). (For interpretation of the references to colour in this figure legend, the reader is referred to the web version of this article.)

by the 8–15 days SMO while that in 2011 was mainly affected by 3–10 days SMO.

The results of the power spectrum analysis on the daily precipitation over HNI obtained from the simulation experiments (Fig. 11) showed that experiment G3 in 2010 and all Group T experiments presented a significant period smaller than that in the actual precipitation power spectrum. The OLR from the experiments passed the power spectrum test was processed with the 8–15 days of filtering. Every experiment performed two northward propagation of oscillation (Fig. 9). Compared with the reality (Fig. 9b), the convection intensity of experiment G3 was smaller, with the center arriving relatively north. The convection intensities were stronger in experiments T1, T2, and T3. The precipitation was simulated best in experiments T4 and T5, in which the timings and intensities of the two northward propagations of oscillation were also best simulated. The first propagation started later in simulation than in reality. However, the arrival time on HNI was in line with the reality.

The second one started from the equator earlier in simulation than in reality. But its arrival time on HNI was the same with reality. The two northward propagations of the 8–15 days convective oscillation were consistent with the processes of the two torrential rain periods (Fig. 9a).

Compared with the reality (Fig. 9a), the simulated precipitation of all Group T experiments showed three similar precipitation processes (Fig. 10). Compared with the reality (Figs. 2 and 4a), the third precipitation process (Figs. 8a and 12) occurred around the surrounding HNI. The timings and intensities of the two northward propagations of precipitation were reproduced best in experiments T4 and T5, which were in line with the reality.

The eastward propagations of the two torrential rains in 2010 (Fig. 13a) were correlated to the northward OLR propagation of the 8–15 days oscillation (Fig. 13b). The timings and intensities of the two eastward propagations of the precipitation and the OLR 8–15 days oscillation were best simulated in experiment T4 and T5 and agreed with

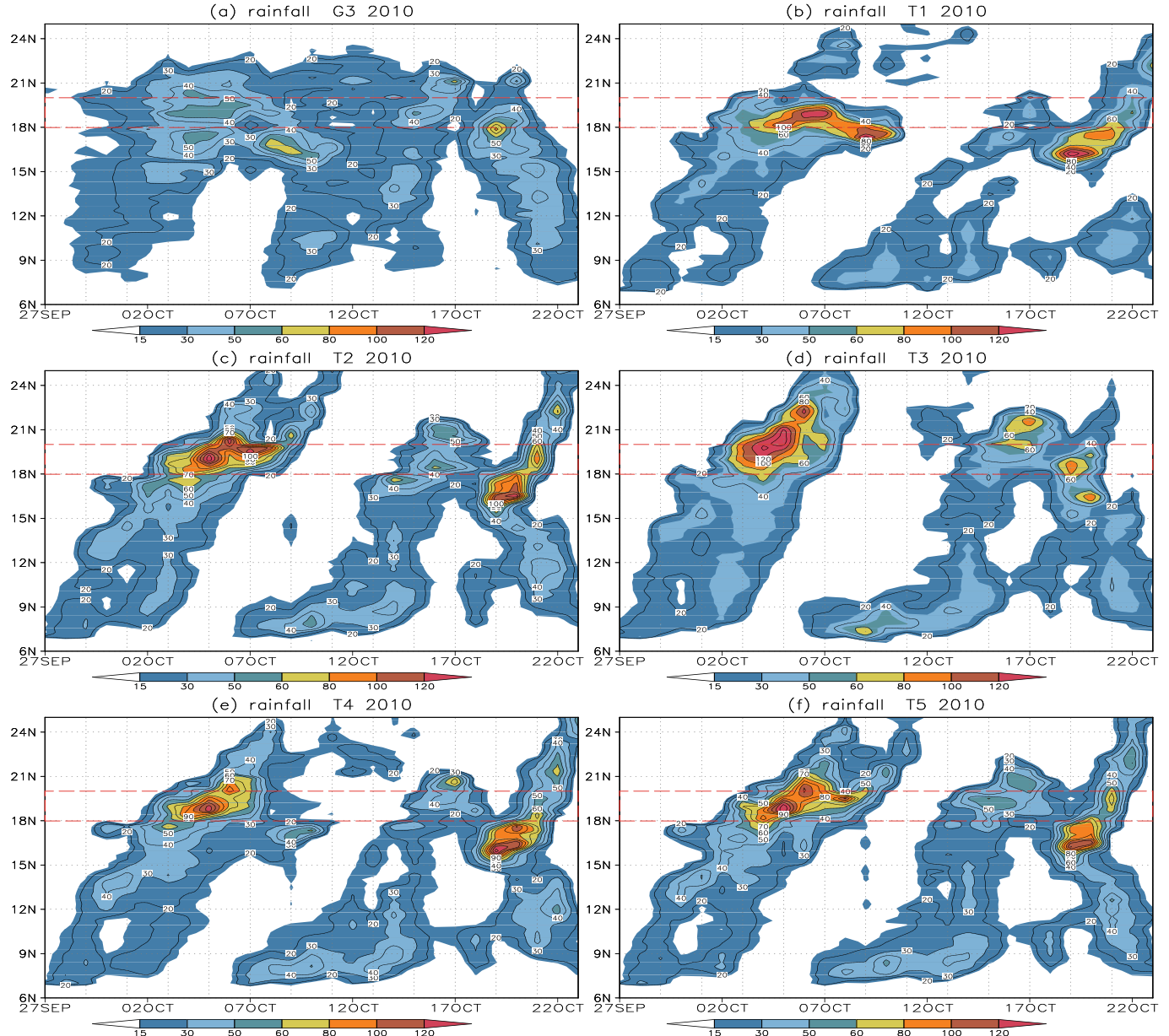


Fig. 12. Time-latitude distributions of averaged daily precipitation (mm) (from D01) in 108°E-120°E for 2010. (a) Experiment G3; (b) Experiment T1; (c) Experiment T2; (d) Experiment T3; (e) Experiment T4; (f) Experiment T5. The red area is HNI. (For interpretation of the references to colour in this figure legend, the reader is referred to the web version of this article.)

the reality (Figs. 13 and 14, respectively).

Experiments G4, T1, T4, and T5 for 2011 (Fig. 15) showed a 3–10 days significant period passing the 90% confidence level. The simulated OLR was processed with 3–10 days filtering (Fig. 15). Experiment G4 presented a poor simulation impact on the two northward propagations of oscillation (Fig. 10c). Experiments T1, T4, and T5 were all able to simulate the northward propagations of the 3–10 days SMO very well. The two northward propagations of the 3–10 days SMO were consistent with the processes of the two torrential rain periods (Fig. 10a), featuring a good precipitation simulation effect.

The westward propagation processes of the two torrential rains in 2011 (Fig. 16a) also corresponded to the OLR 3–10 days oscillation

northward propagation processes (Fig. 16b). Experiment T4 and T5 reproduced the timings and intensities of the two westward propagations of the precipitation and the OLR 3–10 days oscillation the best and were in line with the reality (Figs. 16 and 17, respectively).

Based on the comparison of the two groups of experiments, different CP schemes caused a large difference in the simulation performance of the atmospheric oscillation characteristics. With the same CP schemes, the simulation performances of different CM schemes also varied with negligible difference. Compared the simulated precipitation, the experiments that failed to simulate the characteristics of atmospheric oscillations showed poor performance. Those that captured its periodical characteristics and meanwhile the characteristics of atmospheric

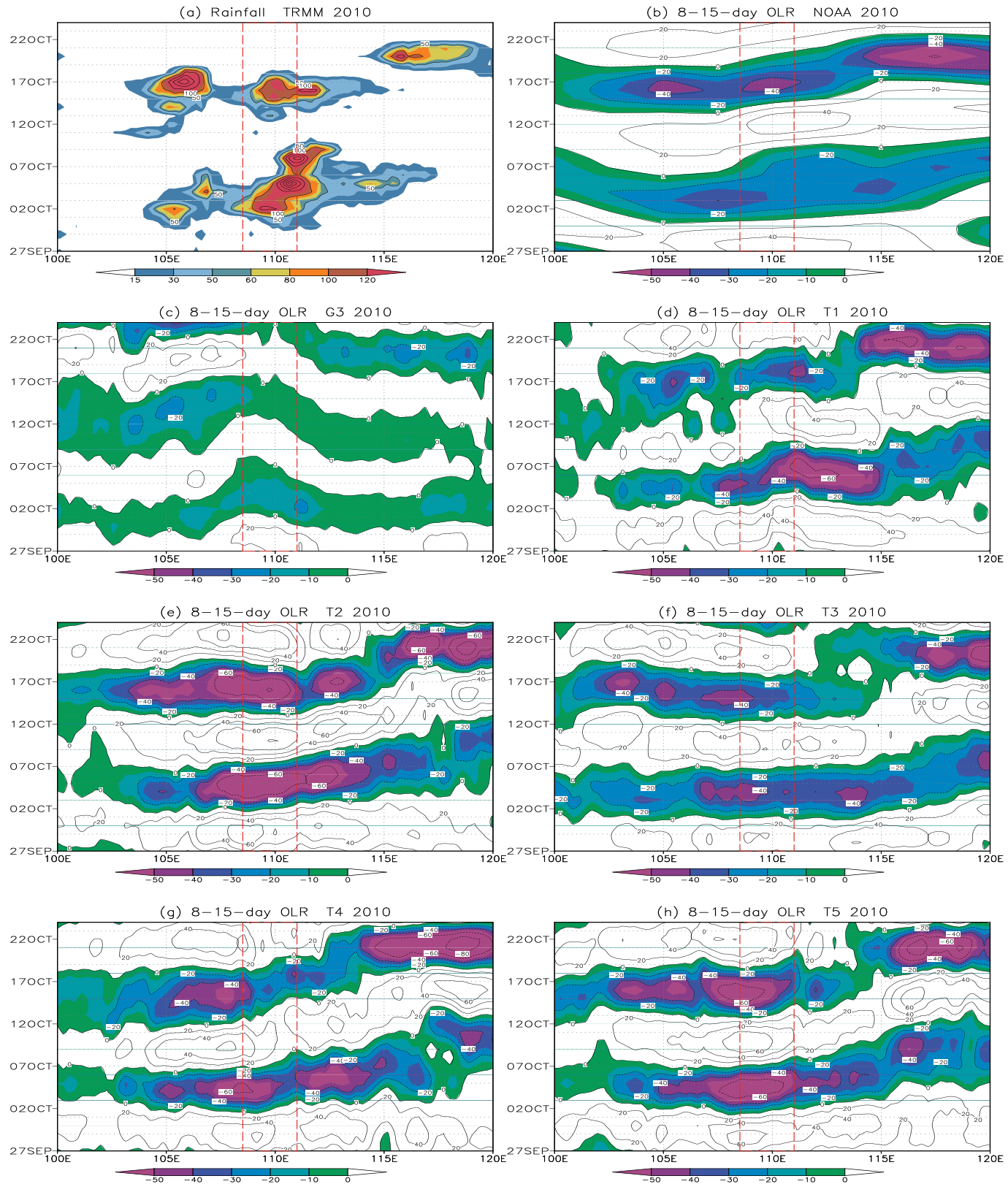


Fig. 13. Time-longitude distributions of averaged daily precipitation (mm) (from D01) and 8–15 days OLR (unit: W·m⁻²) in 18°N–20°N for 2010 (a) Precipitation; (b) NOAA; (c) Experiment G3; (d) Experiment T1; (e) Experiment T2; (f) Experiment T3; (g) Experiment T4; (h) Experiment T5. The red area is HNI. (For interpretation of the references to colour in this figure legend, the reader is referred to the web version of this article.)

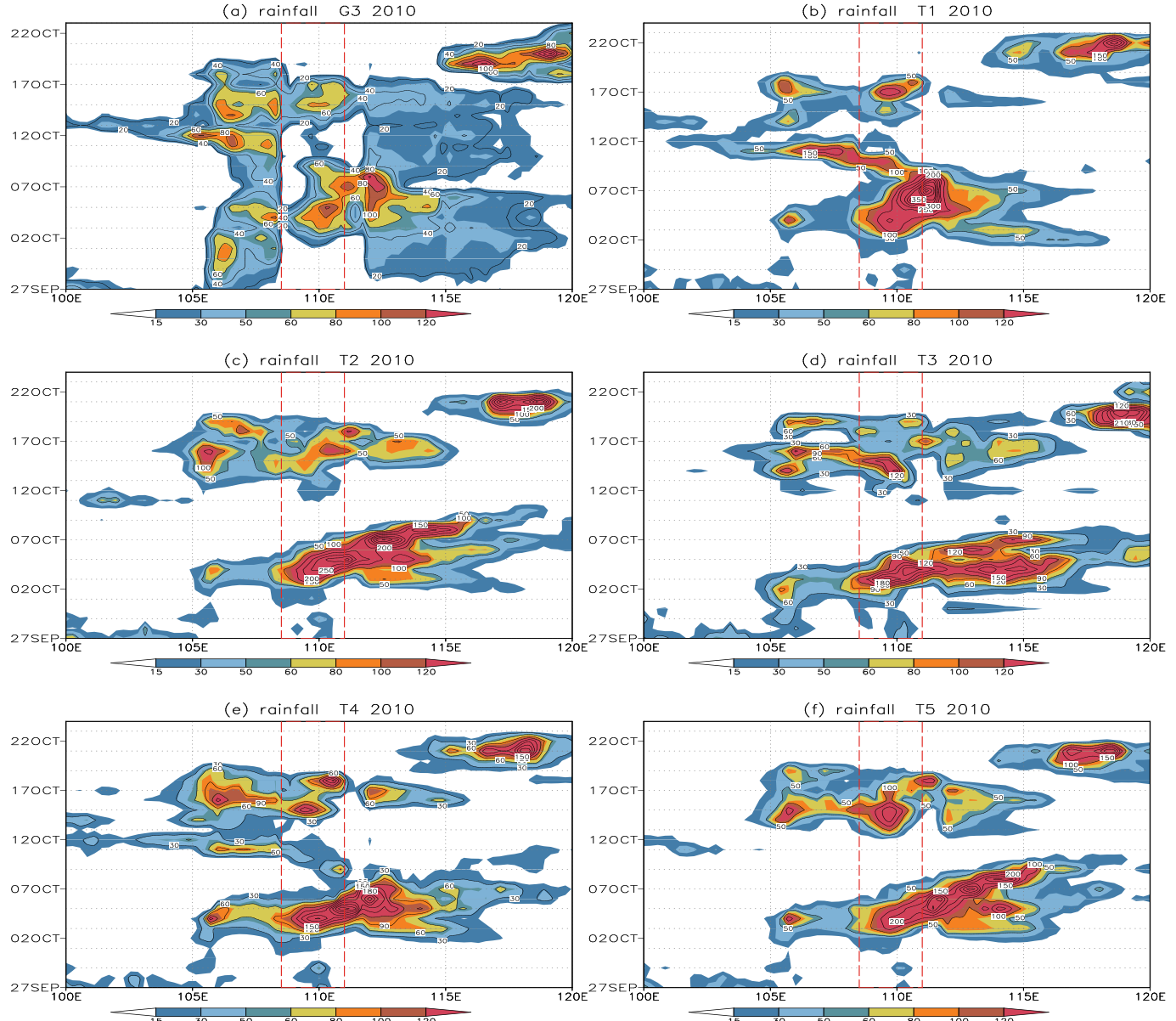


Fig. 14. Time-longitude distributions of averaged daily precipitation (mm) (from D01) in 18°N–20°N for 2010 (a) Experiment G3; (b) Experiment T1; (c) Experiment T2; (d) Experiment T3; (e) Experiment T4; (f) Experiment T5. The red area is HNI. (For interpretation of the references to colour in this figure legend, the reader is referred to the web version of this article.)

oscillation exhibited a better simulation. These results indicated that the CP scheme, the CM scheme, and the atmospheric oscillation exerted significant impact on the two precipitation events during autumn over HNI. The findings indicated the presence of feedback between the MPP and the large-scale environmental field as well.

5. Summary and discussion

In this paper, two groups of monthly-scale simulation experiments were conducted with respect to the two consecutive precipitation periods in autumns of 2010 and 2011 on HNI by using the WRF model. Each group of experiments adopted one CP scheme and five CM schemes, involving five experiments in total. The sensitivity of

simulated consecutive precipitation and SMO to CP schemes and CM schemes was evaluated. We particularly investigated the influence of interaction between MPP and SMO on the autumn precipitation, in which the SMOs included 3–10- and 8–15-day frequency modes.

In the case of the mode using a two-way nested operation, the CP scheme of the large-scale environmental field, which provided boundary conditions for the cloud-scale region, still presented a crucial influence on precipitation. The results from the two groups of experiments showed that the Tiedtke CP scheme presented better simulation results than the Grell–Devenyi CP scheme. Both Tiedtke and Grell–Devenyi CP schemes are the mass flux CP schemes, but The Tiedtke CP scheme is an overall mass flux convection scheme that describes various types of convection, the Grell–Devenyi CP scheme does

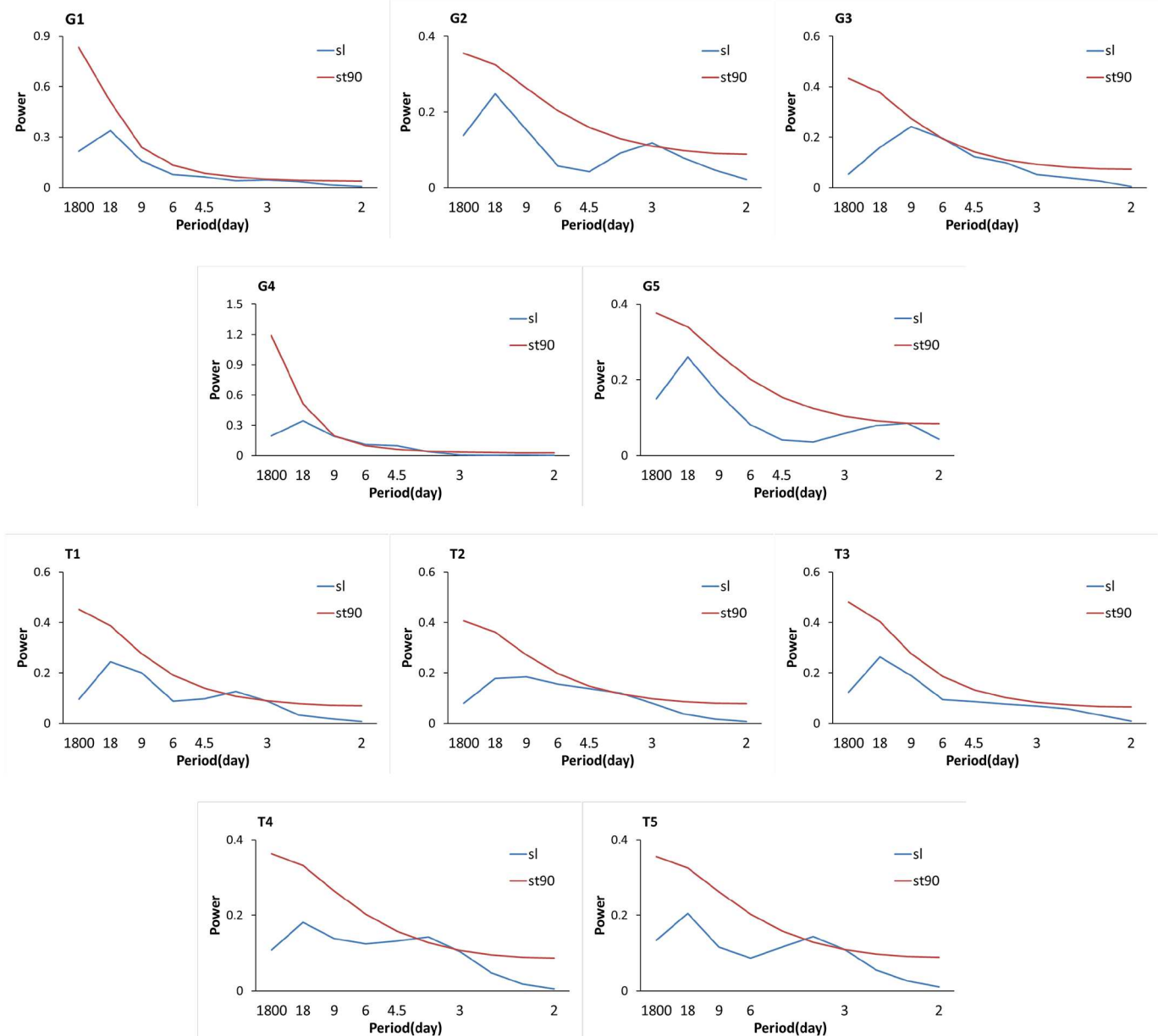


Fig. 15. Power spectrum for average daily simulated precipitation from September 25 to October 24, 2011. (The blue line is the power spectrum, and the red line is the red noise test spectrum, 90% confidence). (For interpretation of the references to colour in this figure legend, the reader is referred to the web version of this article.)

not consider shallow convection. The interaction between clouds and large-scale environment is not detailed enough in it as in the Tiedtke scheme, which affects its simulation performance on SMO. The simulated precipitation in the experiments using the Grell–Devenyi scheme was remarkably less and therefore could not reproduce the precipitation in reality. However, in the same CP scheme, different microphysics schemes also have an impact on simulation performance.

Comparing the results from the two groups of experiments, the simulation results of different CP schemes presented varying simulation performances in terms of the SMO characteristics. In the same CP scheme, the simulation performances of different CM schemes also varied. The experiments that could not simulate the characteristics of SMO presented a poor precipitation simulation, whereas those that

could reflect the characteristics of SMO showed a good precipitation simulation, indicating that the CP scheme, CM scheme, and SMO exerted significant effects on the two heavy rain events on HNI in autumn. A feedback was observed between the MPP and the large-scale environmental field.

With the combination of the Tiedtke CP scheme and the WDM6 CM scheme, the model could reproduce the process of the two strong autumn precipitation events on HNI very effectively. Li et al. (2017) showed that SMO had a significant effect on the two strong autumn precipitation events, but their oscillation characteristics and propagation paths differed. The heavy autumn precipitation of 2010 was mainly dominated by the 8–15-day SMO. The ISO of the two precipitation periods stemmed mainly from the equatorial Indian Ocean region,

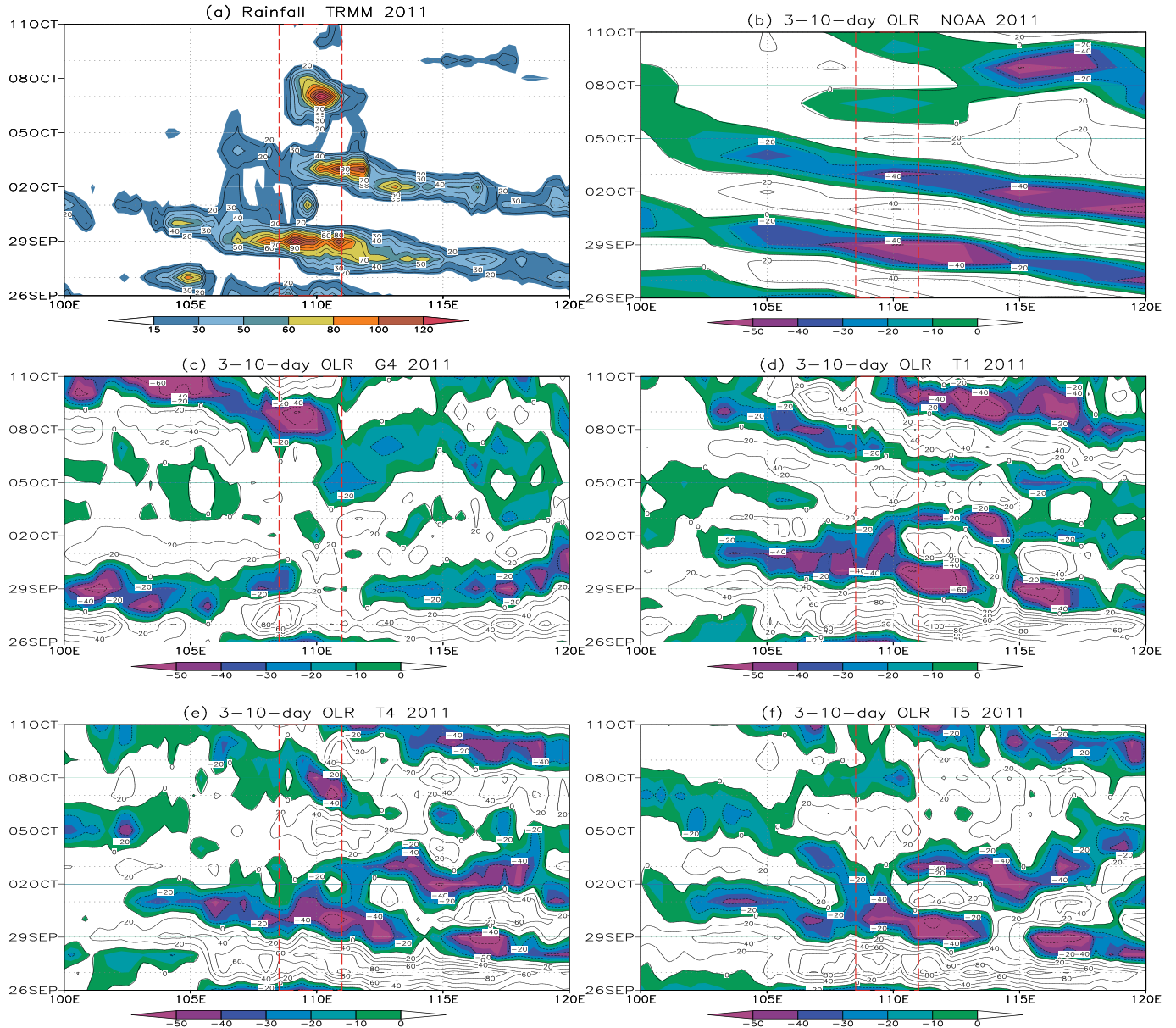


Fig. 16. Time-longitude distributions of averaged daily precipitation (mm) (from D01) and 3–10 days OLR (unit: $\text{W}\cdot\text{m}^{-2}$) in 18°N – 20°N for 2011 (a) Precipitation; (b) NOAA; (c) Experiment G4; (d) Experiment T1; (e) Experiment T4; (f) Experiment T5. The red area is HNI. (For interpretation of the references to colour in this figure legend, the reader is referred to the web version of this article.)

propagated to the northeast, and moved to HNI. The heavy autumn precipitation of 2011 was mainly dominated by the 3–10-day SMO. During the two precipitation periods, the SMO from the Northwest Pacific Ocean propagated to the northwest, near HNI. These simulation results are consistent with the findings of our previous statistical analysis (Li et al., 2017).

Of course, In different stages of the boreal summer, intra-seasonal variability of China precipitation was found to be triggered by dynamic or thermodynamic processes (Liu et al., 2020). The moisture feedback had an effect on the Madden-Julian Oscillation (Liu and Wang, 2017). In this paper, we also found that rainfall on HNI in autumn and SMO are sensitive to MPP. Generally, the Tiedtke scheme is much better in simulating the SMO than the Grell-Devenyi scheme. The main differences between the two CP schemes is that The Tiedtke scheme is an overall

mass flux convection scheme based on the AS-74 scheme (Arakawa and Schubert, 1974) that describes various types of convection. But the Grell-Devenyi scheme does not consider shallow convection, its description of the interaction between clouds and large-scale environment is not detailed enough as the Tiedtke scheme, which affects the dynamic or thermodynamic processes, and also its simulation performance on SMO.

Funding

This study was funded by the National Key Research and Development Program of China under contract No. 2016YFA0602701 and the Jiangsu Collaborative Innovation Center for Climate Change.

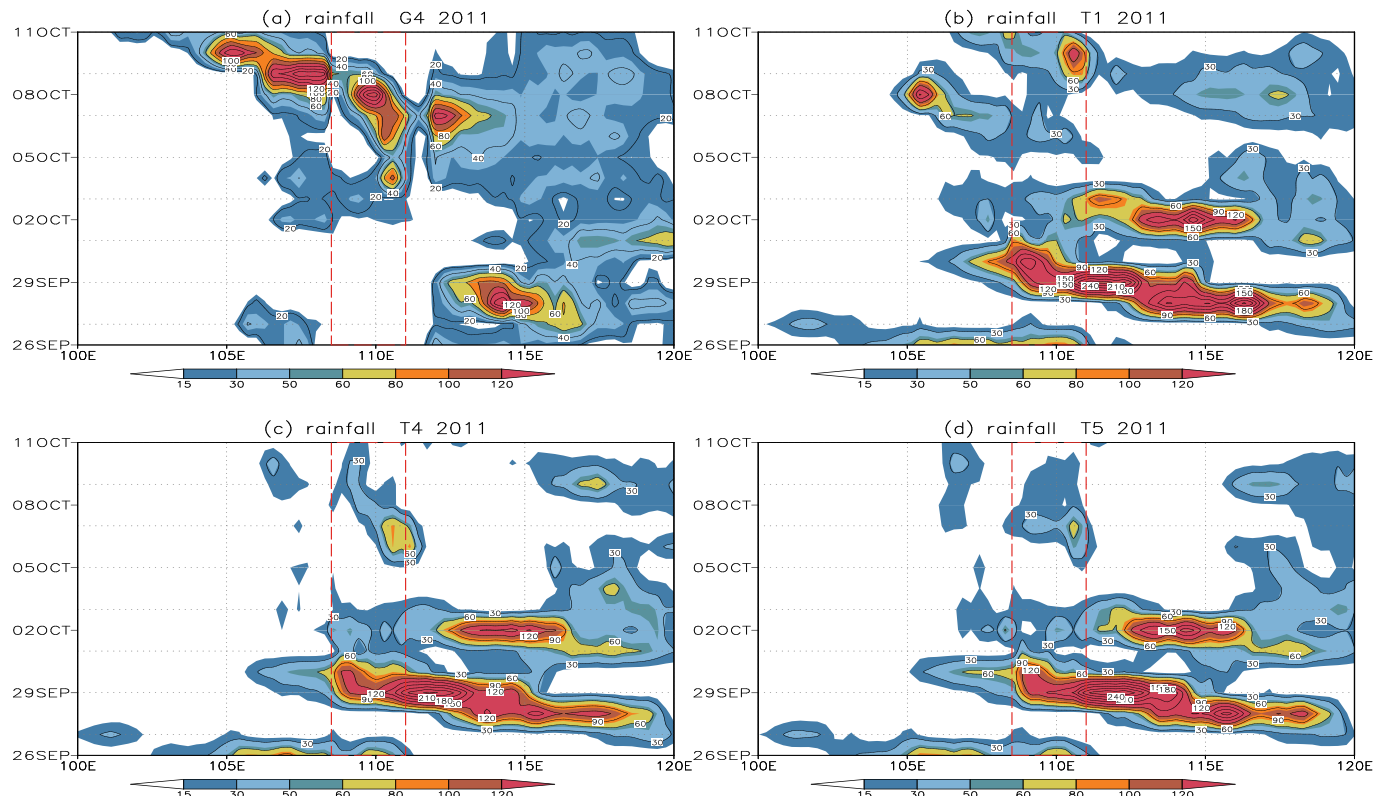


Fig. 17. Time-longitude distributions of averaged daily precipitation (mm) (from D01) in 18°N–20°N for 2011 (a) Experiment G4; (b) Experiment T1; (c) Experiment T4; (d) Experiment T5. The red area is HNI. (For interpretation of the references to colour in this figure legend, the reader is referred to the web version of this article.)

Declaration of Competing Interest

The authors declare that they have no known competing financial interests or personal relationships that could have appeared to influence the work reported in this paper.

References

- Abhilash, S., Sahai, A.K., Borah, N., Chattopadhyay, R., Joseph, S., Sharmila, S., De, S., Goswami, B.N., Kumar, A., 2014. Prediction and monitoring of monsoon intraseasonal oscillations over Indian monsoon region in an ensemble prediction system using CFSv2. *Clim. Dyn.* 42, 2801–2815. <https://doi.org/10.1007/s00382-013-2045-9>.
- Arakawa, A., Schubert, W.H., 1974. Interaction of a cumulus cloud ensemble with the large-scale environment, part I. *J. Atmos. Sci.* 31 (3), 674–701. [https://doi.org/10.1175/1520-0469\(1974\)031<0674:IOACCE>2.0.CO;2](https://doi.org/10.1175/1520-0469(1974)031<0674:IOACCE>2.0.CO;2).
- Blackmon, M.L., 1976. A climatological spectral study of the 500 mb geopotential height of the northern hemisphere. *J. Atmos. Sci.* 33 (8), 1607–1623. [https://doi.org/10.1175/1520-0469\(1976\)033<1607:acssot>2.0.co;2](https://doi.org/10.1175/1520-0469(1976)033<1607:acssot>2.0.co;2).
- Boulard, D., Castel, T., Camberlin, P., Sergeant, A.S., Bréda, N., Badeau, V., Rossi, A., Pohl, B., 2015. Capability of a regional climate model to simulate climate variables requested for water balance computation: a case study over northeastern France. *Clim. Dyn.* 46, 2689–2716. <https://doi.org/10.1007/s00382-015-2724-9>.
- Boulard, D., Castel, T., Camberlin, P., Sergeant, A.S., Asse, D., Bréda, N., Badeau, V., Rossi, A., Pohl, B., 2017. Bias correction of dynamically downscaled precipitation to compute soil water deficit for explaining year-to-year variation of tree growth over northeastern France. *Agric. For. Meteorol.* 232, 247–264. <https://doi.org/10.1016/j.agrformet.2016.08.021>.
- Chao, W.C., Deng, L., 1998. Tropical intraseasonal oscillation, super cloud clusters, and cumulus convection schemes. Part II: 3D aquaplanet simulations. *J. Atmos. Sci.* 55, 690–709. [https://doi.org/10.1175/1520-0469\(1994\)051<1282:TIOSC>2.0.CO;2](https://doi.org/10.1175/1520-0469(1994)051<1282:TIOSC>2.0.CO;2).
- Chen, F., Dudhia, J., 2001. Coupling an advanced land surface-hydrology model with the Penn State-NCAR MM5 modeling system. Part I: model implementation and sensitivity. *Mon. Weather Rev.* 129, 569–585. [https://doi.org/10.1175/1520-0493\(2001\)129<0569:CAALSH>2.0.CO;2](https://doi.org/10.1175/1520-0493(2001)129<0569:CAALSH>2.0.CO;2).
- Chen, G.-S., Liu, Z., Clemens, S.C., Prell, W.L., Liu, X., 2011. Modeling the time-dependent response of the Asian summer monsoon to obliquity forcing in a coupled GCM: a PHASEMAP sensitivity experiment. *Clim. Dyn.* 36, 695–710. <https://doi.org/10.1007/s00382-010-0740-3>.
- Chen, J., Wen, Z., Wu, R., Chen, Z., Zhao, P., 2015. Influences of northward propagating 25–90-day and quasi-biweekly oscillations on eastern China summer rainfall. *Clim. Dyn.* 45, 105–124. <https://doi.org/10.1007/s00382-014-2334-y>.
- Chen, J., Deng, Y., Wang, J., Lin, W., 2017. Hindcasting the Madden-Julian oscillation with a new parameterization of surface heat fluxes. *J. Adv. Model. Earth Syst.* 9, 2696–2709. <https://doi.org/10.1029/2017MS001175>.
- Chen, L., Zhu, C., Wang, W., Zhang, P., 2001. Analysis of the characteristics of 30–60 day low-frequency oscillation over Asia during 1998 SCSMEX. *Adv. Atmos. Sci.* 18, 623–638. <https://doi.org/10.1007/s00376-001-0050-0>.
- Chen, X., Pauluis, O.M., Zhang, F., 2018. Regional simulation of Indian summer Monsoon Intraseasonal Oscillations at Gray Zone Resolution. *Atmos. Chem. Phys.* 18, 1003–1022. <https://doi.org/10.5194/acp-18-1003-2018>.
- Dudhia, J., 1989. Numerical Study of Convection Observed during the Winter Monsoon Experiment using a Mesoscale Two-Dimensional Model. *J. Atmos. Sci.* 46, 3077–3107. [https://doi.org/10.1175/1520-0469\(1989\)046<3077:NSOCOD>2.0.CO;2](https://doi.org/10.1175/1520-0469(1989)046<3077:NSOCOD>2.0.CO;2).
- Evans, J.P., Ekström, M., Ji, F., 2012. Evaluating the performance of a WRF physics ensemble over South-East Australia. *Clim. Dyn.* 39, 1241–1258. <https://doi.org/10.1007/s00382-011-1244-5>.
- Feng, X., Wu, R., Chen, J., Wen, Z., 2013. Factors for Interannual Variations of September–October Rainfall in Hainan, China. *J. Climate* 26 (22), 8962–8978.
- Feng, W., Zhou, L., Xiao, C., Fu, S., 2016. The spatial and temporal characteristics of the autumnal flood season rainfall in Hainan island and its associated circulation features. *J. Trop. Meteorol.* 32 (4), 533–545. <https://doi.org/10.16032/j.issn.1004-4965.2016.04.011>. (In Chinese).
- Gao, J.Y., Hai, L., You, L.J., Si, C., 2016. Monitoring early-flood season intraseasonal oscillations and persistent heavy rainfall in South China. *Clim. Dyn.* 47, 3845–3861. <https://doi.org/10.1007/s00382-016-3045-3>.
- García-Ortega, E., Lorenzana, J., Merino, A., Fernández-González, S., López, L., Sánchez, J.L., 2017. Performance of multi-physics ensembles in convective precipitation events over northeastern Spain. *Atmos. Res.* 190, 55–67.
- Gbode, I.E., Dudhia, J., Ogunjobi, K.O., Ajayi, V.O., 2019. Sensitivity of different physics schemes in the WRF model during a West African monsoon regime. *Theor. Appl. Climatol.* 136, 733–751. <https://doi.org/10.1007/s00704-018-2538-x>.
- Goswami, B.B., Goswami, B.N., 2017. A road map for improving dry-bias in simulating the south Asian monsoon precipitation by climate models. *Clim. Dyn.* 49, 2025–2034. <https://doi.org/10.1007/s00382-016-3439-2>.
- Grell, G.A., Dévényi, D., 2002. A generalized approach to parameterizing convection

- combining ensemble and data assimilation techniques. *Geophys. Res. Lett.* 29, 34–38. <https://doi.org/10.1029/2002GL015311>.
- Ham, S., Hong, S.-Y., 2013. Sensitivity of simulated intraseasonal oscillation to four convective parameterization schemes in a coupled climate model. *Asia-Pacific J. Atmos. Sci.* 49, 483–496. <https://doi.org/10.1007/s13143-013-0043-9>.
- Hayashi, Y., Golder, D.G., 1986. Tropical intraseasonal oscillations appearing in a GFDF general circulation model and FGGE data. Part I: phase Propagation. *J. Atmos. Sci.* 43, 3058–3067. [https://doi.org/10.1175/1520-0469\(1986\)043<3058:TIOAIA>2.0.CO;2](https://doi.org/10.1175/1520-0469(1986)043<3058:TIOAIA>2.0.CO;2).
- Heikkilä, U., Sandvik, A., Sorteberg, A., 2011. Dynamical downscaling of ERA-40 in complex terrain using the WRF regional climate model. *Clim. Dyn.* 37, 1551–1564. <https://doi.org/10.1007/s00382-010-0928-6>.
- Hong, J.-S., 2003. Evaluation of the high-resolution model forecasts over the Taiwan area during GIMEX. *Weather Forecast.* 18, 836–846. [https://doi.org/10.1175/1520-0434\(2003\)018<0836:EOTHMF>2.0.CO;2](https://doi.org/10.1175/1520-0434(2003)018<0836:EOTHMF>2.0.CO;2).
- Hong, S.-Y., Lim, J.-O.J., 2006. The WRF single-moment 6-class microphysics scheme (WSM6). *Asia-Pacific J. Atmos. Sci.* 42, 129–151.
- Hong, S.-Y., Noh, Y., Dudhia, J., 2006. A new vertical diffusion package with an explicit treatment of entrainment processes. *Mon. Weather Rev.* 134, 2318–2341. <https://doi.org/10.1175/MWR3199.1>.
- Hu, W., Duan, A., Wu, G., 2011. Sensitivity of simulated tropical intraseasonal oscillations to cumulus schemes. *Sci. China Earth Sci.* 54, 1761–1771. <https://doi.org/10.1007/s11430-011-4215-0>.
- Huang, A., Zhang, Y., Zhu, J., 2009. Sensitivity of simulation of different intensity of summer precipitation over China to different cumulus convection parameterization schemes. *Chin. J. Atmos. Sci.* 33 (6), 1212–1224. [\(in Chinese\).](https://doi.org/10.3878/j.issn.1006-9895.2009.06.08)
- Huang, Y.-J., Cui, X.-P., Wang, Y.-P., 2016. Cloud microphysical differences with precipitation intensity in a torrential rainfall event in Sichuan, China. *Atmos. Ocean. Sci. Lett.* 9 (2), 90–98.
- Jang, H.-Y., Yeh, S.-W., Chang, E.-C., Kim, B.-M., 2016. Evidence of the observed change in the atmosphere–ocean interactions over the South China Sea during summer in a regional climate model. *Meteorog. Atmos. Phys.* 128, 639–648. <https://doi.org/10.1007/s00703-016-0433-5>.
- Jia, X., Li, C., Zhou, N., Ling, J., 2010. The MJO in an AGCM with three different cumulus parameterization schemes. *Dyn. Atmos. Ocean.* 49, 141–163. <https://doi.org/10.1016/j.dynatmoce.2009.02.003>.
- Jones, C., 2000. Occurrence of extreme precipitation events in California and relationships with the Madden–Julian oscillation. *J. Clim.* 13, 3576–3587. [https://doi.org/10.1175/1520-0442\(2000\)013<3576:OEEPEI>2.0.CO;2](https://doi.org/10.1175/1520-0442(2000)013<3576:OEEPEI>2.0.CO;2).
- Jones, C., Carvalho, L.M., 2014. Sensitivity to Madden–Julian oscillation variations on heavy precipitation over the contiguous United States. *Atmos. Res.* 147, 10–26. <https://doi.org/10.1016/j.atmosres.2014.05.002>.
- Kim, D., Sperber, K., Stern, W., Waliser, D., Kang, I.-S., Maloney, E., Wang, W., Weickmann, K., Benedict, J., Khairoutdinov, M., 2009. Application of MJO simulation diagnostics to climate models. *J. Clim.* 22, 6413–6436. <https://doi.org/10.1175/2009JCLI3063.1>.
- Kim, J.-E., Hong, S.-Y., 2007. Impact of soil moisture anomalies on summer rainfall over East Asia: a regional climate model study. *J. Clim.* 20, 5732–5743. <https://doi.org/10.1175/2006JCLI1358.1>.
- Lau, K.H., Lau, N.C., 1990. Observed structure and propagation characteristics of tropical summertime synoptic scale disturbances. *Mon. Weather Rev.* 118 (9), 1888–1913. [https://doi.org/10.1175/1520-0493\(1990\)1182.0.CO;2](https://doi.org/10.1175/1520-0493(1990)1182.0.CO;2).
- Lau, N.-C., Poshay, J.J., 2009. Simulation of synoptic-and subsynoptic-scale phenomena associated with the East Asian summer monsoon using a high-resolution GCM. *Mon. Weather Rev.* 137, 137–160. <https://doi.org/10.1175/2008mwr2511.1>.
- Li, C.Y., Ling, J., Song, J., Pan, J., Tian, H., Chen, X., 2014. Research progress in China on the tropical atmospheric intraseasonal oscillation. *J. Meteorol. Res.* 28, 671–692. <https://doi.org/10.1007/s13351-014-4015-5>.
- Li, J.N., Wu, K.L., Li, F.Z., Chen, Y.L., Huang, Y.B., 2016. Cloud-scale simulation study on the evolution of latent heat processes of mesoscale convective system accompanying heavy rainfall: the Hainan case. *Atmos. Res.* 169, 331–339. <https://doi.org/10.1016/j.atmosres.2015.10.014>.
- Li, J.N., Ye, Q.W., Li, F.Z., Ding, C.H., Chen, Y.L., Huang, Y.B., 2017. Effects of atmospheric oscillations at different time scales on persistent autumn rainstorms in Hainan, China. *J. Atmos. Solar-Terrestrial Phys.* 164, 243–258. <https://doi.org/10.1016/j.jastp.2017.09.002>.
- Li, J.N., Ye, Q.W., Li, F.Z., Chen, Y.L., 2019. A cloud-resolving simulation study of monthly-scale autumn precipitation on Hainan Island: the effects of three categories of Graupel on rainfall. *Atmos. Res.* 220, 92–108. <https://doi.org/10.1016/j.atmosres.2019.01.008>.
- Li, R.C.Y., Zhou, W., 2015. Multiscale control of summertime persistent heavy precipitation events over South China in association with synoptic, intraseasonal, and low-frequency background. *Clim. Dyn.* 45, 1043–1057. <https://doi.org/10.1007/s00382-014-2347-6>.
- Li, W.B., Wang, D.X., Lei, T., Liu, Z.J., Luo, C., 2011. High-frequency atmospheric variability over South China Sea as depicted by TRMM and QuikSCAT. *Acta Oceanol. Sin.* 30, 46–52. <https://doi.org/10.1007/s13131-011-0104-9>.
- Li, Y., Ju, J., 2009. High-frequency transient and oscillation features related to wet and dry summer monsoons over East China. *Theor. Appl. Climatol.* 95, 165–182. <https://doi.org/10.1007/s00704-007-0373-6>.
- Lim, K.-S.S., Hong, S.-Y., 2010. Development of an effective double-moment cloud microphysics scheme with prognostic cloud condensation nuclei (CCN) for weather and climate models. *Mon. Weather Rev.* 138, 1587–1612. <https://doi.org/10.1175/2009MWR2968.1>.
- Lin, J.-L., Kiladis, G.N., Mapes, B.E., Weickmann, K.M., Sperber, K.R., Lin, W., Wheeler, M.C., Schubert, S.D., Del Genio, A., Donner, L.J., 2006. Tropical intraseasonal variability in 14 IPCC AR4 climate models. Part I: convective signals. *J. Clim.* 19, 2665–2690. <https://doi.org/10.1175/2009MWR2777.1>.
- Lin, Y.-L., Farley, R.D., Orville, H.D., 1983. Bulk parameterization of the snow field in a cloud model. *J. Clim. Appl. Meteorol.* 22, 1065–1092. [https://doi.org/10.1175/1520-0450\(1983\)022<1065:BPOTSF>2.0.CO;2](https://doi.org/10.1175/1520-0450(1983)022<1065:BPOTSF>2.0.CO;2).
- Liu, F., Wang, B., 2017. Effects of moisture feedback in a frictional coupled Kelvin–Rossby wave model and implication in the Madden–Julian oscillation dynamics. *Clim. Dyn.* 48, 513–522. <https://doi.org/10.1007/s00382-016-3090-y>.
- Liu, F., Ouyang, Y., Wang, B., Jian Ling, Hsu, Pang-Chi, 2020. Seasonal evolution of the intraseasonal variability of China summer precipitation. *Clim. Dyn.* <https://doi.org/10.1007/s00382-020-05251-0>.
- Liu, H.-B., Wang, B., 2011. Sensitivity of regional climate simulations of the summer 1998 extreme rainfall to convective parameterization schemes. *Meteorol. Atmos. Phys.* 114, 1. <https://doi.org/10.1007/s00703-011-0143-y>.
- Liu, H.-B., Yang, J., Zhang, D.-L., Wang, B., 2014. Roles of synoptic to quasi-biweekly disturbances in generating the summer 2003 heavy rainfall in East China. *Mon. Weather Rev.* 142, 886–904. <https://doi.org/10.1175/MWR-D-13-00055.1>.
- Madden, R.A., Julian, P.R., 1971. Detection of a 40–50 day oscillation in the zonal wind in the tropical Pacific. *J. Atmos. Sci.* 26, 702–708. [https://doi.org/10.1175/1520-0469\(1971\)028<0702:DOADOI>2.0.CO;2](https://doi.org/10.1175/1520-0469(1971)028<0702:DOADOI>2.0.CO;2).
- Maloney, E.D., Hartmann, D.L., 2000a. Modulation of eastern North Pacific hurricanes by the Madden–Julian oscillation. *J. Clim.* 13, 1451–1460. [https://doi.org/10.1175/1520-0442\(2000\)013<1451:MOENPH>2.0.CO;2](https://doi.org/10.1175/1520-0442(2000)013<1451:MOENPH>2.0.CO;2).
- Maloney, E.D., Hartmann, D.L., 2000b. Modulation of hurricane activity in the Gulf of Mexico by the Madden–Julian oscillation. *Science* 287, 2002–2004. <https://doi.org/10.1126/science.287.5460.2002>.
- Maloney, E.D., Hartmann, D.L., 2001. The sensitivity of intraseasonal variability in the NCAR CCM3 to changes in convective parameterization. *J. Clim.* 14, 2015–2034. [https://doi.org/10.1175/1520-0442\(2001\)014<2015:TSOIVI>2.0.CO;2](https://doi.org/10.1175/1520-0442(2001)014<2015:TSOIVI>2.0.CO;2).
- Mao, J., Wu, G., 2006. Intraseasonal variations of the Yangtze rainfall and its related atmospheric circulation features during the 1991 summer. *Clim. Dyn.* 27, 815–830. <https://doi.org/10.1007/s00382-006-0164-2>.
- Marteau, R., Richard, Y., Pohl, B., Smith, C.C., Castel, T., 2015. High-resolution rainfall variability simulated by the WRF RCM: application to eastern France. *Clim. Dyn.* 44, 1093–1107. <https://doi.org/10.1007/s00382-014-2125-5>.
- Mlawer, E.J., Taubman, S.J., Brown, P.D., Iacono, M.J., Clough, S.A., 1997. Radiative transfer for inhomogeneous atmospheres: RTTM, a validated correlated-k model for the longwave. *J. Geophys. Res. Atmos.* 102, 16663–16682. <https://doi.org/10.1029/97JD00237>.
- Mohan, M., Sati, A.P., 2016. WRF model performance analysis for a suite of simulation design. *Atmos. Res.* 169, 280–291. <https://doi.org/10.1016/j.atmosres.2015.10.013>.
- Morrison, H., Thompson, G., Tatarskii, V., 2009. Impact of cloud microphysics on the development of trailing stratiform precipitation in a simulated squall line: Comparison of one-and two-moment schemes. *Mon. Weather Rev.* 137, 991–1007. <https://doi.org/10.1175/2008MWR2556.1>.
- Moya-Alvarez, A.S., Martínez-Castro, D., Kumar, S., Estevan, R., Silva, Y., 2019. Response of the WRF model to different resolutions in the rainfall forecast over the complex Peruvian orography. *Theor. Appl. Climatol.* 1–15. <https://doi.org/10.1007/s00704-019-02782-3>.
- Pal, J.S., Giorgi, F., Bi, X., Elguindi, N., Solmon, F., Gao, X., Rauscher, S.A., Francisco, R., Zakey, A., Winter, J., 2007. Regional climate modeling for the developing world: the ICPD RegCM3 and RegCNET. *Bull. Am. Meteorol. Soc.* 88, 1395–1410. <https://doi.org/10.1175/BAMS-88-9-1395>.
- Raghavan, S.V., Vu, M.T., Lioung, S.Y., 2016. Regional climate simulations over Vietnam using the WRF model. *Theor. Appl. Climatol.* 126, 161–182. <https://doi.org/10.1007/s00704-015-1557-0>.
- Ren, P., Gao, L., Ren, H., Rong, X., 2019. Representation of the Madden–Julian Oscillation in CAMS-CSM. *J. Meteorol. Res.* 33, 627–650. <https://doi.org/10.1007/s13351-019-8118-x>.
- Ren, X., Yang, X.-Q., Sun, X., 2013. Zonal oscillation of western Pacific subtropical high and subseasonal SST variations during Yangtze persistent heavy rainfall events. *J. Clim.* 26, 8929–8946. <https://doi.org/10.1175/JCLI-D-12-00861.1>.
- Segele, Z., Leslie, L., Tarhule, A., 2015. Sensitivity of horn of Africa rainfall to regional sea surface temperature forcing. *Climate* 3, 365–390. <https://doi.org/10.3390/cli3020365>.
- Segele, Z.T., Leslie, L.M., Lamb, P.J., 2009. Evaluation and adaptation of a regional climate model for the Horn of Africa: rainfall climatology and interannual variability. *Int. J. Climatol.* A J. R. Meteorol. Soc. 29, 47–65. <https://doi.org/10.1002/joc.1681>.
- Seol, K.-H., Hong, S.-Y., 2009. Relationship between the Tibetan snow in spring and the East Asian summer monsoon in 2003: a global and regional modeling study. *J. Clim.* 22, 2095–2110. <https://doi.org/10.1175/2008JCLI2496.1>.
- Skamarock, W.C., Klemp, J.B., 2008. A time-split nonhydrostatic atmospheric model for weather research and forecasting applications. *J. Comput. Phys.* 227, 3465–3485. <https://doi.org/10.1016/j.jcp.2007.01.037>.
- Slingo, J.M., Sperber, K.R., Boyle, J.S., Ceron, J.-P., Dix, M., Dugas, B., Ebisuzaki, W., Fyfe, J., Gregory, D., Gueremy, J.-F., 1996. Intraseasonal oscillations in 15 atmospheric general circulation models: results from an AMIP diagnostic subproject. *Clim. Dyn.* 12, 325–357. <https://doi.org/10.1007/BF00231106>.
- Sperber, K.R., 2004. Madden–Julian variability in NCAR CAM2. 0 and CCSM2. 0. *Clim. Dyn.* 23, 259–278. <https://doi.org/10.1007/s00382-004-0447-4>.
- Srinivas, C.V., Hariprasad, D., Bhaskar Rao, D.V., Anjaneyulu, Y., Baskaran, R., Venkatraman, B., 2013. Simulation of the Indian summer monsoon regional climate using advanced research WRF model. *Int. J. Climatol.* 33, 1195–1210. <https://doi.org/10.1002/joc.3505>.
- Sun, X., Jiang, G., Ren, X., Yang, X., 2016. Role of intraseasonal oscillation in the

- persistent extreme precipitation over the Yangtze River Basin during June 1998. *J. Geophys. Res. Atmos.* 121, 10453–10469. <https://doi.org/10.1002/2016JD025077>.
- Tiedtke, M., 1989. A comprehensive mass flux scheme for cumulus parameterization in large-scale models. *Mon. Weather Rev.* 117, 1779–1800.
- Torrence, C., Compo, G.P., 1998. A practical guide to wavelet analysis. *Bull. Am. Meteorol. Soc.* 79 (1), 61–78. [https://doi.org/10.1175/1520-0477\(1998\)079<0061:APGTWA>2.0.CO;2](https://doi.org/10.1175/1520-0477(1998)079<0061:APGTWA>2.0.CO;2).
- Vitorino, M.I., Dias, P.L.D.S., Ferreira, N.J., 2006. Observational study of the seasonality of the submonthly and intraseasonal signal over the tropics. *Meteorol. Atmos. Phys.* 93 (1–2), 17–35. <https://doi.org/10.1007/s00703-005-0162-7>.
- Wang, C.-C., Kuo, H.-C., Yeh, T.-C., Chung, C.-H., Chen, Y.-H., Huang, S.-Y., Wang, Y.-W., Liu, C.-H., 2013. High-resolution quantitative precipitation forecasts and simulations by the Cloud-Resolving storm Simulator (CReSS) for Typhoon Morakot (2009). *J. Hydrol.* 506, 26–41. <https://doi.org/10.1016/j.jhydrol.2013.02.018>.
- Wang, Hui, Liu, Fei, Wang, Bin, Li, Tim, 2018. Effect of Intraseasonal Oscillation on South China Sea Summer Monsoon Onset. *Clim. Dyn.* 51, 2543–2558. <https://doi.org/10.1007/s00382-017-4027-9>.
- Wang, Qiuyun, Jianping, Li, Yanjie, Li, Xue, Jiaqing, Sen, Zhao, Xu, Yidan, et al., 2019. Modulation of tropical cyclone tracks over the western north pacific by intra-seasonal indo-western pacific convection oscillation during the boreal extended summer. *Clim. Dyn.* <https://doi.org/10.1007/s00382-018-4264-6>.
- Wang, W., Schlesinger, M.E., 1999. The dependence on convection parameterization of the tropical intraseasonal oscillation simulated by the UIUC 11-layer atmospheric GCM. *J. Clim.* 12, 1423–1457. [https://doi.org/10.1175/1520-0442\(1999\)012<1423:TDOCPO>2.0.CO;2](https://doi.org/10.1175/1520-0442(1999)012<1423:TDOCPO>2.0.CO;2).
- Wang, Y., Sen, O.L., Wang, B., 2003. A highly resolved regional climate model (IPRC-RegCM) and its simulation of the 1998 severe precipitation event over China. Part I: model description and verification of simulation. *J. Clim.* 16, 1721–1738. [https://doi.org/10.1175/1520-0442\(2003\)016<1721:AHRCM>2.0.CO;2](https://doi.org/10.1175/1520-0442(2003)016<1721:AHRCM>2.0.CO;2).
- Xiao, F., Wu, R., Chen, J., Wen, Z., 2013. Factors for interannual variations of September–October rainfall in Hainan, China. *J. Clim.* 26, 8962–8978. <https://doi.org/10.1175/JCLI-D-12-00728.1>.
- Yu, Entao, Wang, Huijun, Gao, Yongqi, Sun, Jianqi, 2011. Impacts of cumulus convective parameterization schemes on summer monsoon precipitation simulation over China. *Acta Meteorol. Sin.* 25 (5), 581–592. <https://doi.org/10.1007/s13351-011-0504-y>.
- Zhang, C., 2005. Madden-Julian oscillation. *Rev. Geophys.* 43, RG2003. <https://doi.org/10.1029/2004RG000158>.
- Zhang, C., 2013. Madden-Julian oscillation: Bridging weather and climate. *Bull. Am. Meteorol. Soc.* 94, 1849–1870. <https://doi.org/10.1175/BAMS-D-12-00026.1>.
- Zhang, C., Wang, Y., Hamilton, K., 2011. Improved representation of boundary layer clouds over the Southeast Pacific in ARW-WRF using a modified Tiedtke cumulus parameterization scheme. *Mon. Weather Rev.* 139, 3489–3513. <https://doi.org/10.1175/MWR-D-10-05091.1>.
- Zhang, L., Wang, B., Zeng, Q., 2009. Impact of the Madden-Julian oscillation on summer rainfall in Southeast China. *J. Clim.* 22, 201–216. <https://doi.org/10.1175/2008JCLI1959.1>.
- Zhou, W., Li, C., Chan, J.C.L., 2006. The interdecadal variations of the summer monsoon rainfall over South China. *Meteorol. Atmos. Phys.* 93, 165–175. <https://doi.org/10.1007/s00703-006-0184-9>.
- Zhu, C., Nakazawa, T., Li, J., Chen, L., 2003. The 30–60 day intraseasonal oscillation over the western North Pacific Ocean and its impacts on summer flooding in China during 1998. *Geophys. Res. Lett.* 30, 223–250. <https://doi.org/10.1029/2003GL017817>.